J. Fluid Mech. (1989), vol. 200, pp. 471–509
Printed in Great Britain

Characteristic-eddy decomposition of turbulence in a channel

By PARVIZ MOIN† AND ROBERT D. MOSER‡

† Department of Mechanical Engineering, Stanford University, Stanford, CA 94305, USA *and* NASA Ames Research Center, Moffett Field, CA 94035, USA

‡ NASA Ames Research Center, Moffett Field, CA 94035, USA

(Received 11 January 1988 and in revised form 5 September 1988)

The proper orthogonal decomposition technique (Lumley's decomposition) is applied to the turbulent flow in a channel, to extract coherent structures by decomposing the velocity field into characteristic eddies with random coefficients. In the homogeneous spatial directions a generalization of the shot-noise expansion is used to determine the characteristic eddies. In this expansion the Fourier coefficients of the characteristic eddy cannot be obtained from second-order statistics. Three different techniques are used to determine the phases of these coefficients: (i) a technique based on the bispectrum, (ii) a spatial compactness requirement, and (iii) a functional continuity argument. Results from these three techniques are found to be very similar. The implications of these techniques and the shot-noise expansion are discussed in the Appendix. The dominant eddy is found to contribute as much as 76% to the turbulent kinetic energy. In two and three dimensions, the characteristic eddies consist of an ejection region straddled by streamwise vortices which leave the wall in a very short streamwise distance of approximately 100 wall units.

1. Introduction

The general recognition of the existence of organized motions or eddies in turbulent shear flows can be traced to the works of Theodorsen (1952) and Townsend (1956) over three decades ago. In the past twenty years a great deal of insight has been gained into the characteristics of organized structures in turbulent shear flows primarily by means of flow visualization and conditional-sampling techniques (see Cantwell 1981). Some combined flow visualization and quantitative techniques (e.g. Kline *et al.* 1967; Falco 1977) have demonstrated the significance of certain events (e.g. bursting process) or structures in the turbulence production mechanism.

Unfortunately, the present knowledge of organized motions has seldom been used in turbulence theories or quantitative models of turbulence. This is in part due to the lack of a quantitative definition of organized structures and an objective means for assessing their contribution to turbulence stresses, particularly their importance in the production of turbulence. In addition, most flow visualization studies have been carried out at low Reynolds numbers where the limited range of turbulence scales makes it easier to identify organized motions. Much of our knowledge of coherent motions is limited to those structures that can be *seen* in flow visualization experiments. It is desirable to have the means to extract coherent motions from fields and evaluate their contribution to turbulence statistics, regardless of how chaotic the fields are.

The need for quantitative descriptions of organized structures has led to the use

of statistical techniques. One method, used by Townsend (1956), Grant (1958) Perry & Chong (1982) and others, is to examine measured two-point correlation profiles for their consistency with a proposed structural model. Owing to insufficient experimental data, the conformity of the models with all the components of the two-point correlation tensor has never been investigated. The data are usually deficient in the number of components of the tensor or directions of probe separation. Extrapolation from this insufficient data can lead to confusion. For example, Moin & Kim (1985) have shown that the ability to infer structural information from the two-point correlation profiles is highly dependent on the direction of probe separation. Casual inspection of two-point correlation profiles can also be misleading since one is seeking to extract information on the velocity vector from a tensor.

The conditional or phase-averaging techniques (e.g. the VITA technique of Blackwelder & Kaplan 1976) are statistical methods designed to obtain the average structure that satisfies a prescribed condition, usually at a single point. The difficulty with conditional sampling methods is that the prescribed conditions are generally *ad hoc* and their relevance to actual flow conditions is unclear. Moreover, Adrian & Moin (1988) have shown that the two-point correlation tensor provides a good estimate of conditional velocity fields. Thus, in the neighbourhood of the point at which the conditions are specified, the conditionally averaged velocity can be extracted from the information contained in the correlation tensor.

Most statistical techniques for extraction of organized structures from turbulent flows will produce a 'structure' from virtually any stochastic field, whether or not structures of interest are in the field. Thus, the association of statistically derived structures with instantaneous events of dynamic importance must be predicated on independent knowledge that dynamically significant structures do exist. The result of any such statistical technique is an ensemble *averaged* structure or flow pattern. This flow pattern is often confined to a small section of the flow domain with the surrounding structures averaged out, and the inherent symmetries in the statistics impose 'artificial' symmetries on the resulting structures. Moreover, the interfaces of these structures are generally smeared compared to the edges of instantaneous flow structures. Therefore, averaged structures most likely do not resemble the instantaneous flow structures in detail. The fundamental question is whether the structures deduced by statistical techniques are relevant. This question will be addressed in §6, here we point out that for modelling purposes, one generally is not interested in every detail of the instantaneous structures and the ensemble averaged structure may indeed be what is needed.

In 1967 Lumley proposed a mathematically attractive definition of organized structures and a statistical method for their extraction from stochastic turbulent velocity fields. The method is based on the decomposition of the fluctuating velocity field into a sum of mutually orthogonal eigenfunctions of the two-point correlation tensor, weighted by random coefficients. The dominant (most energetic) eddy is defined to be the eigenfunction with the largest eigenvalue. The Karhunen–Loeve expansion (Loeve 1955; Papoulis 1965) is used in directions in which turbulence is statistically inhomogeneous. This decomposition has also been used for meteorological mapping (Obled & Creutin 1986) and for data compaction and reduction (Ahmed & Rao 1975). An important feature of this decomposition, which results from its orthogonality properties, is that the contribution of the extracted eddies to second-order turbulence statistics can be determined.

There has been scepticism that the long-time averaged, unconditioned two-point correlation tensor used in proper orthogonal decomposition can retain information

about the highly intermittent unsteady structures which have been observed in turbulent wall layers. If a structure, no matter how intermittent, contributes a majority of the total integrated energy or Reynolds stress, then it will dominate the two-point correlation statistics and therefore information about the structure will be retained in the correlation tensor. In fact, it has been shown (Adrian, Moin & Moser 1987) that linear estimates of classical conditional averages (quadrant II), which are computed from the two-point correlation tensor, are in excellent agreement with the actual conditional averages. Thus conditional averaging of this type yields little information which is not available from the two-point correlation tensor. However, if there are several dominant structures with comparable energy, the situation is not clear, and the two-point correlation tensor may not provide adequate information about the structures. Of course, methods for extracting structures from the two-point correlation tensor also suffer from the same difficulties as other statistical methods (e.g. smearing and artificial symmetries). Also, we shall see in §4 that characteristic-eddy decomposition as formulated here is not unique and that external information must be supplied to uniquely determine the Fourier phase coefficients of the resulting characteristic eddies.

Although Lumley's proposal dates back twenty years, it has not been evaluated thoroughly owing to a lack of the necessary experimental data; the complete two-point correlation tensor with at least one direction of probe separation is required. Payne (1966) and Bakewell & Lumley (1967) were the first to apply this technique. Payne (1966) used the two-point correlation measurements of Grant (1958) in the wake of a circular cylinder. Grant measured only the diagonal elements of the two-point correlation tensor, $R_{\alpha\alpha}$, ($\alpha = 1, 2, 3$) at three fixed positions. The remaining off-diagonal correlations were obtained using the mixing-length assumption and the equation of continuity. The energy content of the dominant extracted eddy was not significantly larger than that of the next eigenfunction in the hierarchy. Owing to anomalies in the results, particularly the presence of some negative eigenvalues (which represent the energy content of eddies), these results cannot be considered conclusive. Bakewell & Lumley (1967) applied a simplified version of the decomposition theorem to obtain the most energetic eddy structure in the wall region ($y^+ < 40$) of a turbulent pipe flow. The two-point correlation of the streamwise velocity component, $R_{11}(r_x)$, was measured and decomposed. The other velocity components of the large eddy were obtained using the mixing-length assumption and the equation of continuity. They reported that the largest eddy carries over 90% of the total streamwise turbulent intensity. Moin (1984), who performed the decomposition in only one and two dimensions, was the first to make use of the full correlation tensor. The correlation tensor was obtained from a numerical simulation of turbulent channel flow which made use of a turbulence model to account for the unresolved portion of the turbulence (large-eddy simulation). As in the previous studies, Moin found that the dominant eddy carried much of the turbulent kinetic energy (as much as 64%). Recently, Glauser, Leib & George (1985) applied the scalar decomposition to the streamwise turbulent velocity fluctuations in an axisymmetric turbulent jet. Their results indicate that the dominant eigenfunction carries about 40% of the total streamwise turbulent intensity integrated across the layer.

In recent work by Herzog (1986), the correlation tensor $R_{\alpha\beta}$ was measured in a pipe for $\alpha, \beta = 1$ and 3, the rest of the tensor was reconstructed from the continuity equation. These very ambitious experiments have produced the most comprehensive application of proper orthogonal decomposition to an experimental wall-bounded flow, and are the experiments most directly comparable to the current results.

Herzog's measurements were taken in a small subdomain near the wall, thus they are similar to the near-wall domain decomposition discussed in §5. There are some quantitative differences between Herzog's and the present results. Possible causes for these differences are outlined below. First, Herzog measured the correlation tensor at only six points in the y- and z-directions and seven points in the x-direction; this probably provides an inadequate number of degrees of freedom for the decomposition (see discussion at the end of §3). Further, the spatial resolution of the measured correlation tensor varied greatly in the x- and z-directions, with good resolution for small separations ($\Delta x^+ = 19$ and $\Delta z^+ = 9$) and progressively coarser resolution for larger separations ($x^+ > 40$ and $z^+ > 20$). This necessitated the use of curve-fits to obtain representations of the correlation tensor which could be Fourier transformed. Second, in Herzog's experiment, the correlation was measured using multiple hot-film probes. To preserve the mathematical properties of the correlation tensor, these probes must have identical responses. The fact that they were not identical resulted in some of the eigenvalues being negative, though this was not as serious as in the results of Payne (1966). The use of multiple probes can also lead to probe interference problems. Herzog minimized probe interference by using small probes with slender carriers, but it is still a concern, especially for small spatial separations. Finally, the correlations used for the current results were estimated from a smaller statistical sample than in the experiments, which could lead to some differences due to statistical errors. The impact of these difficulties is not clear. The current results and the results of Herzog are largely in agreement; for example, Aubry & Keefe (1987) found that the individual eigenfunctions they examined were quite similar in shape. However, there are some significant differences (see §§3 and 5). The extent to which the differences are caused by the cited difficulties is a matter of speculation. Other potential causes of these differences are the difference between a pipe and channel, and the fact that Herzog's pipe flow was not fully developed.

The objective of the present work is to extract the characteristic eddies, as defined by Lumley's decomposition, in fully developed turbulent channel flow and measure their contribution to turbulence statistics. The characteristic eddies are those with maximal contribution to turbulent kinetic energy, but the theory does not maximize their contribution to the turbulence production mechanism (i.e. Reynolds shear stress). One of the results of this study is the contribution of the extracted eddies to the turbulent shear stress profile.

A major difficulty with the decomposition technique is the treatment of the homogeneous directions, in which the Karhunen–Loeve decomposition is not useful. Lumley (1981) proposed using a generalization of the shot-noise decomposition (Rice 1944). However, there is considerable arbitrariness in the specification of this decomposition. In Lumley's approach, the magnitudes of the Fourier coefficients of the decomposition are found easily, but the phases are more difficult. Lumley (1981) recommends using the third-order moments in the form of the bispectra to recover the phases. This proposal has not previously been implemented. One of the objectives of this study is to use additional statistical data to retrieve the phase information and compare the characteristics of the dominant structure to those obtained with other techniques. Some of the implications of using different specifications of the shot-noise decomposition have also been studied.

The necessary statistical data are obtained from a database generated by direct numerical simulation of turbulent channel flow (Kim, Moin & Moser 1987). This database consists of instantaneous three-dimensional velocity and pressure fields collected at widely separated flow times. Calculations were performed at Reynolds

number 3200 based on the centreline velocity, U_0, and channel half-width, δ. The channel centreline corresponds to $y^+ = yu_\tau/\nu = 180$, where $u_\tau = (\tau_w/\rho)^{\frac{1}{2}}$ is the wall shear velocity. The computations were carried out with $128 \times 129 \times 128$ grid points in the x-, y- and z-directions respectively. The mean flow is in the x-direction and y is in the direction normal to the walls. Total averaging time was about $190\delta/U_0$. The physical realism of the data has been verified by detailed comparison of statistical correlations and both instantaneous and conditionally averaged flow patterns with available experimental data.

In §2 the procedure for calculation of the two-point spectral-density tensor is outlined. In §3 the inhomogeneous turbulence decomposition or Karhunen–Loeve expansion in the direction normal to the walls and its computational implementation is presented. In §4 the theoretical aspects of the shot-noise decomposition in the homogeneous directions are discussed. The characteristic eddy decomposition is applied in two and three dimensions in §5, and the structure of resulting dominant eddies are examined, followed by conclusions and a general discussion in §6.

2. Calculation of two-point spectral-density tensor

Application of the orthogonal decomposition theorem to turbulent channel flow with one direction of flow inhomogeneity and two homogeneous directions requires the knowledge of the two-point spectral-density tensor. This tensor is calculated from the direct simulation database described in §1. The Karhunen–Loeve expansion requires the two-point velocity-correlation tensor,

$$R_{ij}(r_x, y, y', r_z) = \langle u_i(x, y, z, t)\, u_j(x+r_x, y', z+r_z, t)\rangle, \tag{2.1}$$

where u_i $(i = 1, 2, 3)$ are the instantaneous turbulent velocity fluctuations in the streamwise, x, normal, y, and spanwise, z, directions respectively. The $\langle\ \rangle$ denotes ensemble average which, owing to flow homogeneity in x- and z-directions, is calculated by averaging in (x, z)-planes as well as in time. It is actually more convenient to compute and use the two-point spectral-density tensor $\Phi_{ij}(k_x, y, y', k_z)$ which is the Fourier transform of the two-point correlation tensor in r_x and r_x, that is

$$\Phi_{ij}(k_x, y, y', k_z) = \frac{1}{4\pi^2}\iint \mathrm{e}^{-\mathrm{i}k_x r_x - \mathrm{i}k_z r_z} R_{ij}(r_x, y, y', r_z)\,\mathrm{d}r_x\,\mathrm{d}r_z, \tag{2.2}$$

where k_x and k_z are the wavenumbers in the x- and z-directions.

For computational purposes, the discrete Fourier transform of each instantaneous velocity field has been computed:

$$\hat{u}_i(k_z, y, k_z, t_n) = \sum_{x,z} u_i(x, y, z, t_n)\,\mathrm{e}^{-\mathrm{i}k_x x - \mathrm{i}k_z z}. \tag{2.3}$$

The two-point spectral density is obtained from

$$\Phi_{ij}(k_x, y, y', k_z) = \frac{1}{N_t}\sum_{n=1}^{N_t} \hat{u}_i(k_x, y, k_z, t_n)\,\hat{u}_j^*(k_x, y', k_z, t_n), \tag{2.4}$$

where N_t is the number of instantaneous flow fields used for ensemble averaging and * denotes complex conjugate. Since Φ_{ij} is the Fourier transform of R_{ij}, a real function, it is conjugate symmetric,

$$\Phi_{ij}(k_x, y, y', k_z) = \Phi_{ij}^*(-k_x, y, y', -k_z). \tag{2.5}$$

The Navier–Stokes equations, and the boundary conditions in the channel flow are invariant with respect to two coordinate transformations, a reflection in the z-direction (z mapped to $-z$ and w becomes $-w$), and a reflection in the y-direction about the centreline. For each velocity field in the ensemble, the velocity field obtained by any combination of these reflections is also included in the ensemble, since they are equally valid solutions of the Navier–Stokes equations. This effectively quadruples the statistical sample and exactly enforces the following two symmetries in Φ_{ij} ($y = 0$ at the centreline):

$$\Phi_{ij}(k_x, y, y', k_z) = \pm \Phi_{ij}(k_x, -y, -y', k_z), \tag{2.6a}$$

$$\Phi_{ij}(k_x, y, y', k_z) = \pm \Phi_{ij}(k_x, y, y', -k_z). \tag{2.6b}$$

In (2.6a) the minus sign is used for $i = 2$ or $j = 2$ but not both, while in (2.6b), the minus sign is used for $i = 3$ or $j = 3$ but not both. The symmetry in (2.6b) also results in a factor-of-two reduction in the computation required to perform the proper orthogonal decomposition in three dimensions. Finally, Φ_{ij} has the following symmetry due to its definition:

$$\Phi_{ij}(k_x, y, y', k_z) = \Phi^*_{ji}(k_x, y', y, k_z). \tag{2.7}$$

These symmetries, and others which can be derived by combining them, will be used throughout the sections that follow.

3. The Karhunen–Loeve expansion in the inhomogeneous direction

A preliminary evaluation of the decomposition theorem can be performed by using the decomposition of the correlation tensor, $R_{ij}(y, y')$, for two points separated only in the inhomogeneous direction (y). This decomposition, known as the Karhunen–Loeve expansion (Loeve 1955; Papoulis 1965), is the foundation of the characteristic-eddy decomposition for multiple dimensions presented in the next section. Note that while the decomposition may be performed in one or more dimensions, the underlying turbulent flow is always three-dimensional and time dependent. The material presented below leading to equations (3.1)–(3.7) can be found in Lumley (1970). It is presented here for continuity.

Let $v_i(y)$ be a random vector function on a finite domain D. Given an ensemble of realizations of v_i, we wish to determine a deterministic vector function (or *organized structure*), $\phi_i(y)$, that has the highest possible mean-square correlation with the members of the ensemble. That is, we wish to find $\phi_i(y)$ that maximizes the ensemble average of the magnitude squared of the quantity

$$\alpha = \frac{\int_D v_i(y)\,\phi_i^*(y)\,\mathrm{d}y}{\left(\int_D \phi_l(y)\,\phi_l^*(y)\,\mathrm{d}y\right)^{\frac{1}{2}}}. \tag{3.1}$$

Unless otherwise stated, in this paper the summation convention is implied for repeated indices. Note that in the above inner product only the shape and not the magnitude of ϕ_i is considered. It can be shown (Lumley 1970) by the methods of calculus of variation that the desired ϕ is a solution (eigenfunction) of

$$\int_D R_{ij}(y, y')\,\phi_j^*(y')\,\mathrm{d}y' = \lambda \phi_i(y), \tag{3.2}$$

where $R_{ij} = \langle v_i(y)\, v_j(y') \rangle$ is the two-point correlation function and $\langle\ \rangle$ denotes ensemble average. It can be shown that (3.2) does not have a unique solution; instead there is a denumerable infinity of solutions, $\phi_i^{(n)}(y)$, which can be normalized such that

$$\int_D \phi_i^{(n)}(y)\, \phi_i^{(m)*}(y)\, \mathrm{d}y = \delta_{nm}. \tag{3.3}$$

Orthogonality implies that structures of different order do not interact with each other in their contribution to second-order statistics. Each eigenfunction $\phi_i^{(n)}(y)$ is associated with a real positive eigenvalue $\lambda^{(n)}$, and the eigenfunctions form a complete set. That is, the random vector field v_i, can be reconstructed from the eigenfunctions

$$v_i(y) = \sum_n a_n\, \phi_i^{(n)}(y), \tag{3.4}$$

where coefficients of different order are uncorrelated,

$$\langle a_n\, a_m^* \rangle = \begin{cases} \lambda^{(n)} & (n = m), \\ 0 & (n \neq m). \end{cases} \tag{3.5}$$

Equation (3.4) is interpreted as the decomposition of the stochastic field v_i into deterministic elements (or eddies) with random coefficients. It is expected that more deterministic velocity fields will be more efficiently represented by the expansion (3.4). An important consequence of (3.5) is that the contribution of each structure to the turbulent kinetic energy and turbulence stresses can be determined:

$$\langle v_i(y)\, v_j(y) \rangle = \sum_n \lambda^{(n)} \phi_i^{(n)}(y)\, \phi_j^{(n)}(y), \tag{3.6}$$

and

$$E = \int_D \langle v_i\, v_i \rangle\, \mathrm{d}y = \sum_n \lambda^{(n)}, \tag{3.7}$$

where E is the total turbulence kinetic energy in the domain. The eigenvalues $\lambda^{(n)}$ thus represent the contribution of each structure to the total turbulent kinetic energy.

It should be pointed out that the Karhunen–Loeve expansion can be formulated for any subdomain, $y_1 \leqslant y \leqslant y_u$. In this case the limits of the integrals in (3.2), (3.3) and (3.7) are changed to y_1 and y_u and the eigenfunctions represent the characteristic structures in that subdomain. The division of the full domain of interest into two or more smaller regions may be advantageous for the convergence of the expansion and provide the means for further dissection of the flow field in a given region. For example, in turbulent boundary layers we may wish to find the characteristic structures in the wall and outer layers separately, rather than search for one global structure for the entire flow. This is consistent with the general treatment of the problem of multiple scales in turbulent boundary layers.

The above formalism is applied to the three-dimensional time-dependent velocity field, $u_i(x, y, z, t)$, in turbulent channel flow. Our aim is to find the optimum representation, in the statistical sense outlined above, of the velocity field in the direction y normal to the walls. That is, given the velocity profiles $u_i(y)$ at all the (x, z)-locations and at all times, we seek deterministic functions that optimally represent the y-variation of the velocity field. The desired ϕ_i are obtained by substituting into (3.2) the two-point correlation tensor $R_{ij}(y, y')$ defined in (2.1) with

$r_x = r_z = 0$. The integral equation (3.2) is solved numerically. The numerical approximation to the integral in (3.2) is given by

$$\int_D f(y)\,\mathrm{d}y \approx \sum_{i=1}^{N} \omega_i f_i, \tag{3.8}$$

where f_i is the value of f at a discrete grid point and ω is the weight function for the particular quadrature method used. In the present work we have used the trapezoidal rule with up to $N = 129$ non-uniformly spaced grid points for the entire domain, $-1 \leqslant y \leqslant 1$. The grid points are given by

$$y_j = -\cos\left[\frac{\pi(j-1)}{(N-1)}\right] \quad (j = 1, 2, \ldots, N).$$

The numerical approximation of the integral in (3.2) leads to an algebraic eigenvalue problem

$$\boldsymbol{A}\boldsymbol{\phi}^{(n)} = \lambda^{(n)}\boldsymbol{\phi}^{(n)}, \tag{3.9}$$

where $\boldsymbol{A}$ is a $3N \times 3N$ matrix and

$$\boldsymbol{\phi}^{(n)} = [\phi_1^{(n)}(1), \phi_2^{(n)}(1), \phi_3^{(n)}(1), \ldots, \phi_1^{(n)}(N), \phi_2^{(n)}(N), \phi_3^{(n)}(N)]^{\mathrm{T}}$$

is the discretized nth eigenvector (of dimension $3N$), with $\phi_1^{(n)}(i)$ the streamwise component of the nth eigenfunction at the ith grid point. Because of the use of non-uniformly spaced grid-points, $\boldsymbol{A}$ is not symmetric. However, a simple scaling transformation using the diagonal matrix with the diagonal, $D = [(\omega_1)^{\frac{1}{2}}, (\omega_1)^{\frac{1}{2}}, (\omega_1)^{\frac{1}{2}}, \ldots, (\omega_N)^{\frac{1}{2}}, (\omega_N)^{\frac{1}{2}}, (\omega_N)^{\frac{1}{2}})]$ transforms (3.9) into a symmetric eigenvalue problem.

The numerical integration in (3.8) could have also been done using the Chebyshev polynomial representation used in the simulations of Kim *et al.* (1987), which would have been more accurate. The trapezoidal rule was selected because it allows much greater flexibility in solving the problem in subdomains. Use of the trapezoidal rule is justified because the correlation tensor is much smoother than the instantaneous velocity fields.

It can be easily proven that the discrete system (3.9) preserves all the essential properties of its continuous counterpart given by (3.2), all the eigenvalues are real and positive, the eigenvectors are orthonormal when the discrete analogue of (3.3) is formed using the same quadrature rule used to approximate the integral in (3.2). In addition, the relations (3.4)–(3.7) are also exactly satisfied when the discretized instantaneous velocity fields are represented in terms of the eigenvectors of $\boldsymbol{A}$. These properties serve as a good check of the computer implementation of the method. It can also be shown for both the analytical and numerical problem that the eigenfunctions will satisfy the same boundary conditions as the velocity and that in the three-dimensional decomposition (see §4) the eigenfunctions will satisfy continuity (including $\partial v/\partial y = 0$ at the wall).

In this paper the eigenvalues will be arranged in descending order with $\lambda^{(1)}$ as the largest eigenvalue. We shall refer to $\phi^{(1)}$ as the 'dominant' eigenfunction or eddy. Whether $\phi^{(1)}$ is indeed *dominant* depends on the magnitude of $\lambda^{(1)}$ relative to the magnitude of the remainder of the eigenvalue spectrum. This must be determined from the computations. For the one-dimensional formulation discussed in this section the spanwise component of each eigenfunction, $\phi_3^{(n)}$, is uncoupled from its streamwise and normal components. This is a reflection of the fact that for $(i = 1, 2)$, R_{3i}, R_{i3} are zero Therefore, in the remainder of this section, $\phi_3^{(m)}$ denotes the spanwise component of the mth eigenfunction with zero streamwise and vertical components,

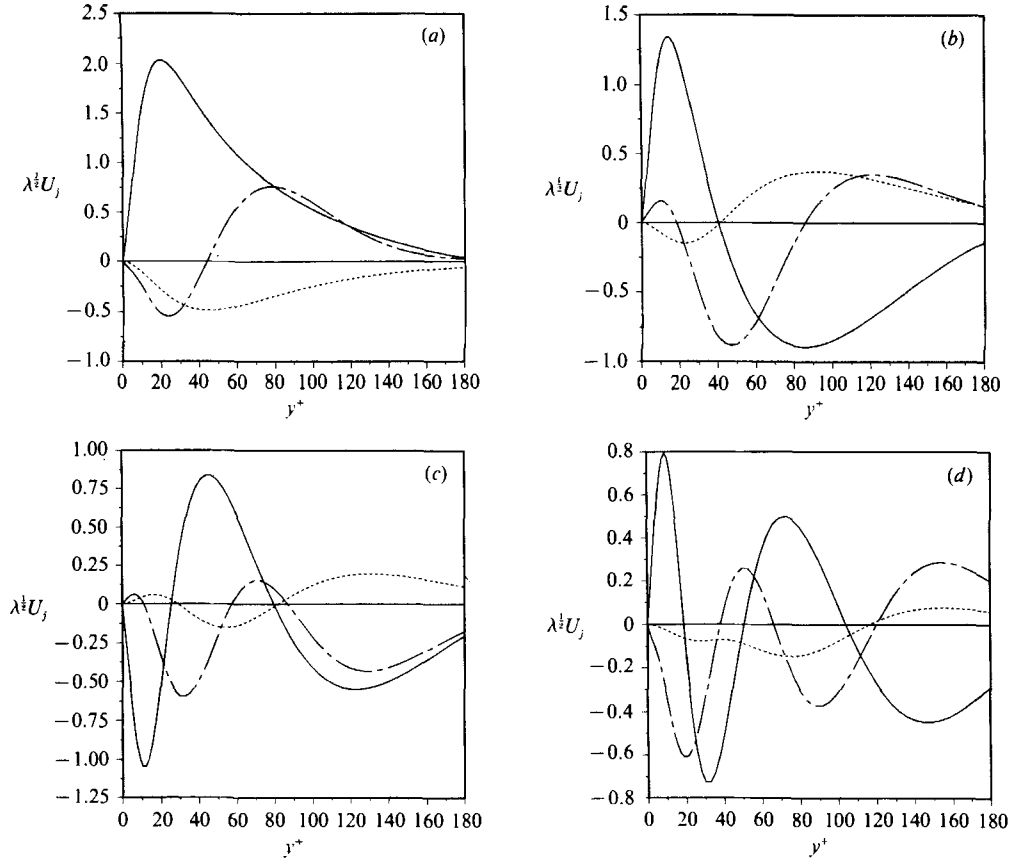

FIGURE 1. First four one-dimensional eigenfunctions in the wall-to-centreline domain: ——, streamwise velocity (u); · · · · · ·, normal velocity (v); — — —, spanwise velocity (w). (a) First, (b) second, (c) third and (d) fourth eigenfunction.

and $\phi_1^{(l)}$ and $\phi_2^{(l)}$ denote the streamwise and vertical components of the lth eigenfunction with zero spanwise component. However, when we refer to the total energy, E, it is the sum of all $3N$ of the eigenvalues. In the multidimensional formulation discussed in the next section all three components of each eigenfunction are fully coupled.

The first four eigenfunctions for the domain extending from the wall to the centreline of the channel ($0 \leqslant y^+ \leqslant 180$) are shown in figure 1. Note that the eigenfunctions are normalized to have a magnitude of unity, in accordance with (3.6); however, in figure 1, they are multiplied by $(\lambda^{(n)})^{\frac{1}{2}}$ to allow comparison of their relative contributions to turbulent stresses. The Karhunen–Loeve eigenfunctions generally behave in the same manner as other typical eigenfunctions, namely, the number of zero-crossings increases with the order of the eigenfunction. It is particularly significant that the streamwise, $\phi_1^{(n)}$, and vertical, $\phi_2^{(n)}$, components of the first three eigenfunctions have opposite signs throughout the domain and, hence, make a positive contribution to turbulence production. This is not the case for some of the higher-order eigenfunctions. It is also interesting that $\phi_3^{(1)}(y)$ changes sign in the vicinity of the wall. A streamwise vortex located near the wall yields a spanwise velocity profile, w, that is similar to $\phi_3^{(1)}$.

Domain	N_D	$\lambda^{(1)}/E$	$\lambda^{(2)}/E$	$\lambda^{(3)}/E$	$\lambda^{(1)}/\lambda^{(2)}$	$P^{(1)}/P^{(t)}$
$0 \leqslant y^+ \leqslant 40$	29	0.61	0.15	0.08	4.2	1.03
$140 \leqslant y^+ \leqslant 180$	10	0.44	0.22	0.20	2.0	1.94
$0 \leqslant y^+ \leqslant 180$	65	0.32	0.16	0.08	2.0	0.66

TABLE 1. Contributions of the one-dimensional eigenfunctions to energy and production

The contributions of the first three eigenfunctions to the total turbulent kinetic energy (equation (3.7)) in three separate domains are shown in table 1. The contribution of the dominant eigenfunction to turbulent shear stress and hence turbulence production in each domain is indicated by the quantity $P^{(1)}/P^{(t)}$, where $P^{(1)}$ is the integral of the first term in (3.6) with $i = 1, j = 2$,

$$P^{(1)} = \lambda^{(1)} \int_{y_l}^{y_u} \phi_1^{(1)} \phi_2^{(1)} \, \mathrm{d}y,$$

and $P^{(t)}$ is the integral of the total turbulence shear stress

$$P^{(t)} = \int_{y_l}^{y_u} \langle u_1 u_2 \rangle \, \mathrm{d}y.$$

For the domain extending from the wall to the channel centreline the dominant eigenfunction makes an appreciable contribution to the total turbulence kinetic energy, and its contribution to turbulence production is remarkably high. For the wall layer ($y^+ \leqslant 40$) the contributions of the first eigenfunction to both turbulent kinetic energy and production are very significant. For all the cases tabulated the dominant eigenfunction's contribution to turbulence shear stress is significantly higher than its contribution to turbulent kinetic energy. Note that the first eigenfunction may contribute more than 100% of the Reynolds shear stress. While the formulation guarantees that convergence to the energy and the turbulence intensities is monotonic, there is no such guarantee for the Reynolds shear stress. In fact, the decomposition emphasizes the shear stress of the lower eigenfunctions, requiring higher-order eigenfunctions to contribute negatively to the Reynolds shear stress. In contrast, Herzog (1986) obtained Reynolds shear stress contributions which were less than 100% and did converge monotonically. The reason for this difference is not known (see the discussion of Herzog's experiment in §1).

The convergence of the Karhunen–Loeve (K–L) expansion for turbulence stresses as a function of the number of terms in (3.6) for the wall-to-centreline domain is shown in figure 2. Note that in this figure and the convergence plots shown in figure 3 the solid curve labelled 'total' is the Reynolds stress taken from the direct numerical simulation of Kim *et al.* (1987). All velocities are non-dimensionalized with the wall shear velocity, u_τ. The high Reynolds shear stress content of the lower-order eigenfunctions is clearly evident. It appears that approximately 10 terms in the expansion are required to reproduce the turbulence stresses with a reasonable accuracy. Note that for this case the matrix $\boldsymbol{A}$ (equation (3.9)) is 195×195 and possesses 195 orthonormal eigenvectors.

The convergence of the expansion in the wall-layer ($y^+ \leqslant 40$) is shown in figure 3. The convergence is remarkably fast; three to five terms in (3.6) are sufficient to reproduce all the turbulence stresses. In this case the matrix $\boldsymbol{A}$ is 87×87. The convergence of any expansion in a subdomain is expected to be better than that in the entire domain. However, as shown in table 1 the Karhunen–Loeve expansion

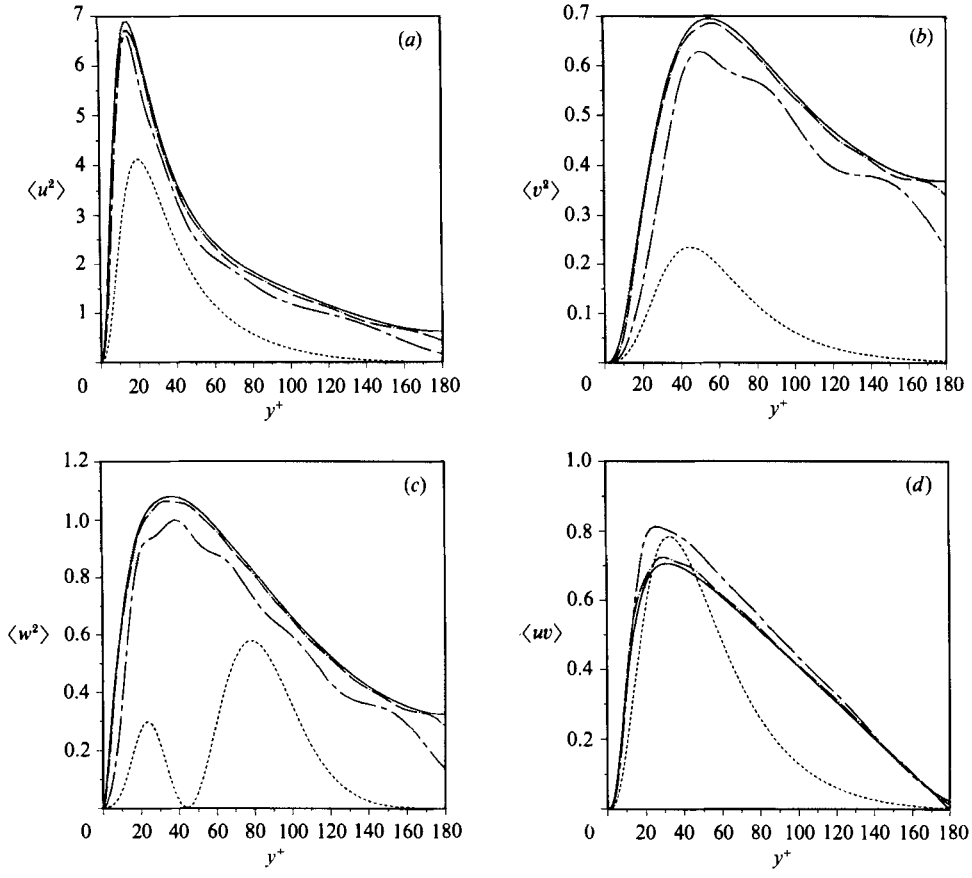

FIGURE 2. Convergence of (*a*) u^2, (*b*) v^2, (*c*) w^2 and (*d*) uv in the wall-to-centreline domain: ——, total; · · · · · ·, first eigenfunction: — — —, sum of first (*a*) 5, (*b*) 10, (*c*) 5 and (*d*) 5 eigenfunctions; —·—, sum of first (*a*) 10, (*b*) 20, (*c*) 10 and (*d*) 10 eigenfunctions.

converges faster in the wall layer than in a subdomain of the same size away from the wall, despite the fact that turbulence quantities vary most rapidly in the wall region. A possible explanation for better convergence of the wall-layer eigenfunctions is that turbulence motions near a wall are more organized (deterministic) than outer-layer turbulence resulting in a larger projection α in (3.1).

The disparity of scales between the wall and outer layer suggests that better convergence may be obtained if the entire domain is split into two or more regions and the eigenfunctions for each region calculated separately. To verify this assertion, the wall-to-centreline domain was split into the two parts, $y^+ \leqslant 40$ and $40 < y^+ \leqslant 180$, and for each case (3.2) was solved. The sum of the contributions of the dominant eigenfunction from each region is 45% of the total kinetic energy as compared to 32% when the domain was not split. No attempt was made to optimize the y-location at which the domain was split.

Each velocity component has an alternative expansion that can be obtained by solving (3.2) with only the autocorrelation of that velocity component. For example streamwise, eigenfunctions can be obtained from

$$\int_D R_{11}(y, y')\varphi^*(y')\,\mathrm{d}y' = \lambda\varphi(y). \tag{3.10}$$

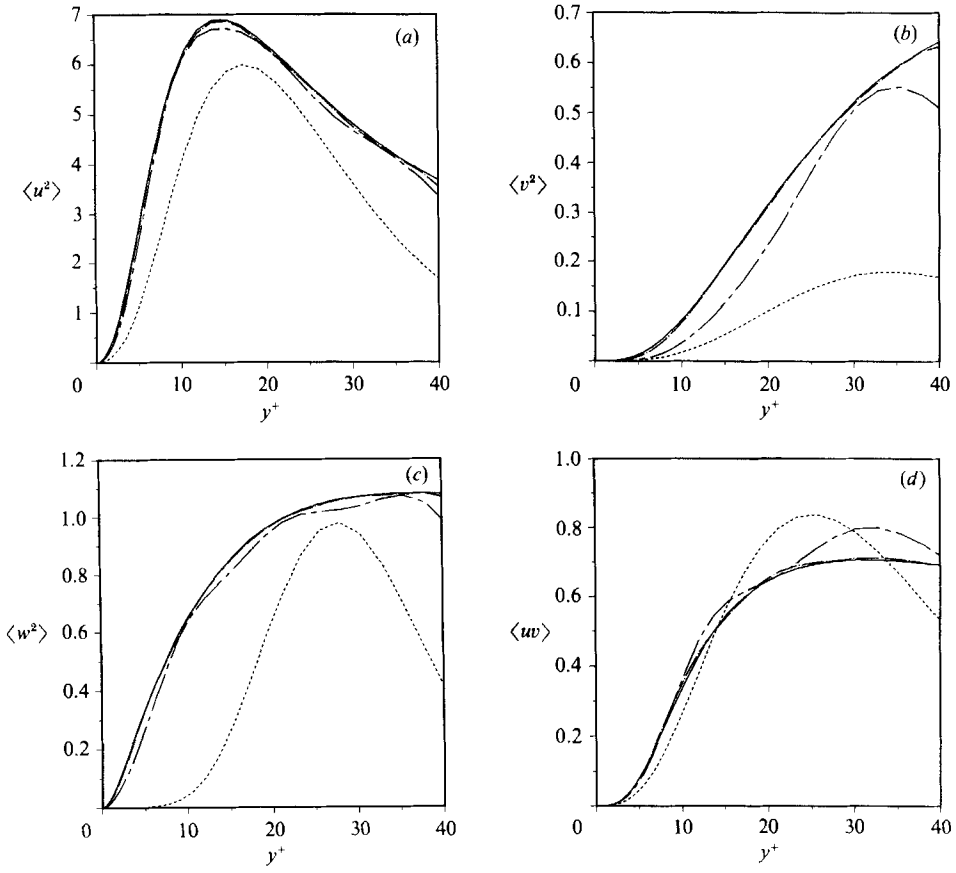

FIGURE 3. Convergence of (*a*) u^2, (*b*) v^2, (*c*) w^2 and (*d*) uv in the near-wall domain: ——, total; – – –, first eigenfunction; · · · · · ·, sum of first (*a*) 3, (*b*) 5, (*c*) 3 and (*d*) 3 eigenfunctions; —·—, sum of first (*a*) 5, (*b*) 10, (*c*) 5 and (*d*) 5 eigenfunctions.

Such an expansion for each velocity component clearly has a faster convergence rate than the one obtained from the full decomposition. For example, (3.10) was solved for the near-wall domain, and the dominant eigenfunction's contribution is 74% of the total streamwise turbulent intensity. However, scalar decompositions for each component of the velocity fluctuations do not reveal any information about the contribution of the eigenfunctions to the Reynolds shear stress.

Since the convergence of the Karhunen–Loeve expansion in representing energy is optimal, it is of interest to see how its convergence compares with that of the Chebyshev polynomials which are used in performing direct numerical simulations. To that end, the streamwise velocity component was decomposed in the full domain from one wall to the other by obtaining the eigenvalues of (3.10). These are compared with the energy carried by partial sums of the Chebyshev polynomials in the representation of the streamwise velocity fluctuations. The power of the Karhunen–Loeve expansion is evident in the first term; the first eigenfunction carries 23% of the energy, whereas the first Chebyshev polynomial carries only 4%. However, when one considers the number of terms required to represent the energy to a given tolerance, the performance difference is not as impressive. For example, to represent 90% of the energy, 10 eigenfunctions and 12 Chebyshev polynomials are

required and to represent the energy to one part in 10^3, 35 eigenfunctions and 42 Chebyshev polynomials are needed. Thus the Karhunen–Loeve expansion is significantly advantageous if only one or two terms are to be retained; however, for accurate simulations of the type performed by Kim *et al.* (1987), the small improvement in accuracy obtained by using the Karhunen–Loeve expansion would not offset the increased computational cost such a scheme would entail.

Finally, one should be cautious in drawing conclusions regarding the convergence of the expansions when using too few grid points in (3.2) or measuring R_{ij} at only a few points y. This has often been the case in experimental measurements of two-point correlations (e.g. Herzog 1986). Eigenvectors of (3.9) form a basis for a space of vectors of dimensions $3N_D$, where N_D is the number of grid points in the domain. Thus, the number of terms in (3.6) required to recover all the turbulent kinetic energy at the grid points is always less than or equal to $3N_D$. One can be confident that a sufficient number of points has been used only if the number of terms required for convergence is significantly less than $3N_D$. Note that for scalar decompositions such as (3.10) the corresponding turbulent intensity at the grid points is recovered (by default) with less than or equal to N_D terms in the expansion. In table 1 the number of grid points in each domain is shown.

4. Theory of characteristic eddies in multiple dimensions

The one-dimensional Karhunen–Loeve expansion described in §3 provided some guidance to the significance of the 'dominant' eigenfunction. The merit of this decomposition is evident in the wall layer where the dominant eigenfunction is indeed the major contributor to turbulence kinetic energy and production. However, eigenfunctions in one dimension do not represent eddies; and application of the decomposition method to the problem of identifying organized structures in turbulent flows requires its implementation in more than one dimension, so that the shape of the extracted eddy as well as its contribution to turbulent stresses can be determined. In this section we consider the theoretical foundations of the three-dimensional decomposition, with two spatial directions (x and z) homogeneous. A two-dimensional decomposition can be developed similarly.

For the three-dimensional case we wish to determine the eigenfunctions of the three-dimensional two-point correlation tensor $R(r_x, y, y', r_z)$, where r_x and r_z are separations in the homogeneous directions x and z. Since the Karhunen–Loeve eigenfunctions in homogeneous spatial directions are the Fourier functions (Lumley 1981), we can equivalently consider the following eigenvalue problem:

$$\int_D \Phi_{ij}(k_x, y, y', k_z)\,\hat{\phi}_j^*(k_x, y', y, k_z)\,\mathrm{d}y' = \lambda(k_x, k_z)\,\hat{\phi}_i(k_x, y, k_z), \tag{4.1}$$

where Φ_{ij} is the spectral-density tensor discussed in §2. The Karhunen–Loeve eigenfunctions are then $\hat{\phi}_i(k_x, y, k_z)\exp(\mathrm{i}k_x x + \mathrm{i}k_z z)$. These are not acceptable as characteristic eddies because the Fourier functions are not local in space, and we expect the eddies to be spatially compact. Moreover, the Fourier eigenfunctions are the eigenfunctions for *any* statistically homogeneous system so they do not reflect properties related to turbulence structure. The homogeneous spatial directions require a different treatment which, following Lumley (1981), will be based on a generalization of the shot-noise decomposition (Rice 1944).

The eigenfunctions of (4.1) have all the properties of the eigenfunctions developed

in §3. In particular eigenfunctions of different order are orthogonal and they can be normalized so that

$$\int \hat{\phi}_i^{(n)}(k_x, y, k_z)\, \hat{\phi}_i^{(m)*}(k_x, y, k_z)\, \mathrm{d}y = \delta_{nm}, \tag{4.2}$$

and the Fourier transform of the velocity field can be reconstructed from the eigenfunctions with random uncorrelated coefficients

$$\hat{u}_i(k_x, y, k_z) = \sum_n \hat{a}_n(k_x, k_z)\, \hat{\phi}_i^{(n)}(k_x, y, k_z), \tag{4.3a}$$

and

$$\langle \hat{a}_n(k_x, k_z)\, \hat{a}_m^*(k_x, k_z) \rangle = \begin{cases} \lambda^{(n)}(k_x, k_z) & \text{for } n = m, \\ 0 & \text{for } n \neq m. \end{cases} \tag{4.3b}$$

Note that the normalization condition (4.2) sets the magnitude of the complex eigenfunction $\hat{\phi}_i$ but leaves the phase unspecified; the phases may be set arbitrarily.

To obtain the shot decomposition in the homogeneous directions, consider the first term in (4.3) for each k_x and k_z:

$$\hat{u}_i^{(1)}(k_x, y, k_z) = \hat{a}_1(k_x, k_z)\, \hat{\phi}_i^{(1)}(k_x, y, k_z), \tag{4.4}$$

which is the 'dominant' term of the inhomogeneous decomposition, and has the maximum contribution to the kinetic energy at each wavenumber. Equation (4.4) can be inverse Fourier transformed to obtain

$$u_i^{(1)}(x, y, z) = \int \phi_i^{(1)}(x-x', y, z-z')\, a_1(x', z')\, \mathrm{d}x'\, \mathrm{d}z'. \tag{4.5}$$

The inverse transform of the coefficients $\hat{a}_1$ is a_1 which can be interpreted as a stochastic process in the homogeneous spatial directions, and the deterministic function $\phi_i^{(1)}$ is the inverse transform of the first eigenfunctions for each wavenumber. This is the form of the generalized shot decomposition, in which the deterministic function $\phi_i^{(1)}$ would be interpreted as a characteristic eddy which is distributed randomly in the homogeneous spatial directions ('sprinkled' or 'scattered') by the stochastic process a_1. However, the Fourier transform of $\phi_i^{(1)}$ obtained from (4.1) and (4.2) has arbitrary amplitude (set arbitrarily by the normalization condition in (4.2)) and phase, and is therefore inappropriate as a characteristic eddy.

To determine these quantities for the characteristic eddy (ϕ_i^c), we seek a generalized shot decomposition of $u_i^{(1)}$,

$$u_i^{(1)}(x, y, z) = \int \phi_i^c(x-x', y, z-z')\, g(x', z')\, \mathrm{d}x'\, \mathrm{d}z', \tag{4.6}$$

where the magnitudes and phases of the characteristic eddy are determined by some objective criteria, and g is the stochastic 'sprinkling' process. The characteristic eddy ϕ_i^c can be related to $\phi_i^{(1)}$ in (4.6), and g can be related to a_1 by the following relations:

$$\phi_i^c(x, y, z) = \int \phi_i^{(1)}(x-x', y, z-z') f(x', z')\, \mathrm{d}x'\, \mathrm{d}z', \tag{4.7a}$$

and

$$a_1(x, z) = \int f(x-x', z-z')\, g(x', z')\, \mathrm{d}x'\, \mathrm{d}z', \tag{4.7b}$$

where f is a deterministic function. Equation (4.7b) can also be interpreted as a generalized shot decomposition of the homogeneous stochastic process a_1. There are

several subtleties to the decomposition (4.6) and the criteria by which the Fourier magnitudes and phases of ϕ_i^c are determined. In particular, there are many criteria that could be used to define the decomposition, so that this decomposition is not unique. The criteria actually used to obtain the results presented in §5 are discussed briefly in the following paragraphs; the Appendix contains further discussion of this subject.

To determine the magnitudes of the Fourier coefficients of f and therefore ϕ_i^c, we require that g is 'white' in the sense that the integral of g in non-overlapping intervals is uncorrelated (Lumley 1981). This property determines the second-order statistics of the process g, which is assumed to have zero mean:

$$\langle g(x,z)\, g(x',z')\rangle = \delta(x-x', z-z'), \tag{4.8a}$$

and

$$\langle \hat{g}(k_x,k_z)\, \hat{g}^*(k_x',k_z')\rangle = \delta(k_x-k_x', k_z-k_z'). \tag{4.8b}$$

Obviously, g could be multiplied by any constant, which would only change the scaling of f. Other conditions on g or f are possible (see the Appendix); however, this is an appealing choice, since it makes the second-order statistics of g primitive. The function f then carries the second moment of a_1,

$$\langle a_1(x,z)\, a_1(x+\delta x, z+\delta z)\rangle = \int f(x,z) f(x+\delta x, z+\delta z)\, \mathrm{d}x\, \mathrm{d}z. \tag{4.9}$$

Taking the Fourier transform and recalling (4.3b), the spectrum of f is obtained:

$$|\hat{f}(k_x,k_z)|^2 = \lambda^{(1)}(k_x,k_z). \tag{4.10}$$

The Fourier magnitudes of $\hat{f}$ and therefore ϕ_i^c are thus determined; however, the phases of $\hat{f}$ cannot be determined from the second-order statistics of g and a_1.

Though the phases do not affect the contribution of the characteristic eddies to second-order statistics, they do determine the physical structure of the eddies. Results shown in §5 use three different methods to find the phases. The first method makes use of the third-order statistics of the stochastic processes a_1 and g, as suggested by Lumley (1981). In the second method, the characteristic eddy is required to be compact in space in a sense to be discussed below. The third method makes use of the fact that for continuous wavenumbers (infinite computational domain), it is expected that the Fourier components of ϕ_i^c would be continuous functions of the wavenumbers. These methods are discussed below.

4.1. *Phase determination from the bispectrum*

To make use of the third-order statistics of a_1 and g we follow Lumley (1981) and consider the bispectrum. The bispectrum of a stochastic process g, B_g, is the Fourier transform of the three-point correlation function, R_g (see Lii, Rosenblatt & Van Atta 1976; Van Atta 1979; Elgar & Guza 1985). We have

$$R_g(r_x,r_x',r_z,r_z') = \langle g(x,z)\, g(x+r_x,z+r_z)\, g(x+r_x',z+r_z')\rangle, \tag{4.11a}$$

and

$$B_g(k_x,k_x',k_z,k_z') = \langle \hat{g}(k_x,k_z)\, \hat{g}(k_x'k_z')\, \hat{g}^*(k_x+k_x',k_z+k_z')\rangle. \tag{4.11b}$$

Using the Fourier transform of (4.7b) and (4.10), the bispectrum of a_1 and that of g can be related:

$$B_{a_1}(k_x,k_x',k_z,k_z') = B_g(k_x,k_x',k_z,k_z')[\lambda^{(1)}(k_x,k_z)\,\lambda^{(1)}(k_x',k_z')\,\lambda^{(1)}(k_x+k_x',k_z+k_z')]^{\frac{1}{2}} \times \exp\{\mathrm{i}[\theta(k_x,k_z)+\theta(k_x',k_z')-\theta(k_x+k_x',k_z+k_z')]\}, \tag{4.12}$$

where $\theta(k_x, k_z)$ is the phase of $\hat{f}(k_x, k_z)$ (i.e. $\hat{f}(k_x, k_z) = [\lambda^{(1)}(k_x, k_z)]^{\frac{1}{2}} \exp[\mathrm{i}\theta(k_x, k_z)]$). We would like to require that B_g be a real positive constant. This is analogous to the 'whiteness' property imposed on the second-order statistics of g, and implies that g has primitive third-order moments in the sense discussed above (see the Appendix for further discussion). It is not possible to impose this condition however, because (4.12) completely determines the magnitude of B_g for all wavenumbers, and B_g will not in general be constant. The condition that B_g be real and positive requires that

$$\psi(k_x, k_x', k_z, k_z') = \theta(k_x, k_z) + \theta(k_x', k_z') - \theta(k_x + k_x', k_z + k_z'), \tag{4.13}$$

where ψ is the phase of B_{a_1}, which would allow the determination of the phases θ. However, in general, (4.13) has no solution since it represents order-N^2 equations for the order-N unknown θ values, where N is the total number of Fourier modes. Instead we shall require that (4.13) be satisfied approximately. This problem is encountered in optics, seismology and signal analysis (Bartelt, Lohmann & Wirnitzer 1984; Matsuoka & Ulrych 1984), and a variety of solution techniques have been proposed. For the results presented in §5, equation (4.13) was solved in a weighted least-squares sense, where the weights are taken to be the magnitude of the bispectrum of a_1. However, for the two-dimensional decomposition, the phases were constrained to take on values of 0 or π (see below).

For two-dimensional decompositions (y and z), the symmetries of the flow result in a simplification of the bispectrum. The symmetries of Φ_{ij} shown in (2.5) and (2.6*b*) imply in the two-dimensional case that

$$\Phi_{ij}(y, y', k_z) = \pm \Phi_{ij}^*(y, y', k_z), \tag{4.14}$$

where the plus and minus signs are as in (2.6*b*). This implies that Φ_{ij} is strictly real unless $i = 3$ or $j = 3$ (but not both), in which case it is pure imaginary. This in turn implies that the eigenfunctions $\hat{\phi}_i(y, k_z)$ are strictly real for $i = 1, 2$ and pure imaginary for $i = 3$. To compute the bispectrum of a_1, the realizations of a_1 must be determined from u; this is done by using (4.3*a*) and the orthogonality of the eigenfunctions to obtain

$$\hat{a}_1(k_z) = \int \hat{u}_i(y, k_z)\, \hat{\phi}_i^{(1)*}(y, k_z)\, \mathrm{d}y. \tag{4.15}$$

It is easily shown that when (4.15) is used to compute a_1 from the velocity field and a_1' from the z-reflection of the velocity field (as discussed in §2), the special properties of the eigenfunction discussed above imply that

$$\hat{a}_1(k_z) = \hat{a}_1'^*(k_z). \tag{4.16}$$

The bispectrum of a_1 can be expressed as

$$B_{a_1}(k_z, k_z') = \langle \hat{a}_1(k_z)\, \hat{a}_1(k_z')\, \hat{a}_1^*(k_z + k_z') \rangle. \tag{4.17}$$

The ensemble in this average includes velocity fields and their z-reflection as discussed in §2, which with equation (4.16) implies that the bispectrum B_{a_1} is real. Referring to (4.12), it is easily seen that if the phase of $\hat{f}$ is 0 or π for all k_z (i.e. $\hat{f}$ is real for all k_z), then the bispectrum of g will also be real for all k_z and k_z', as desired. Also, it is clear from (4.13) that if γk_z is added to any solution for $\theta(k_z)$, it will remain a solution. This simply represents a shift of the characteristic eddy in the z-direction. Thus the problem of finding the phases $\theta(k_z)$ of $\hat{f}$ reduces to finding the sign of $\hat{f}$. In the weighted least-squares solution of (4.13), the values of $\theta(k_z)$ are restricted to be 0 or π, so that the bispectrum of g remains real. The least-squares problem reduces

to determining the sign of $\hat{f}(k_z)$ such that $\Sigma_{k_z k_z'} B_g(k_z, k_z') |B_{a_1}(k_z, k_z')/B_g(k_z, k_z')|$ is maximum. This was solved by a discrete steepest ascent algorithm.

4.2. *Phase determination from a compactness condition*

Given the magnitude of $\hat{f}$ as determined from (4.10), the phases can be determined by imposing a condition on ϕ_i^c rather than g. In particular, we use the fact that when we speak of an eddy in a turbulent field, we mean a structure that is compact in space. This requirement of spatial compactness is one of the reasons the Fourier functions were rejected as characteristic eddies. The compactness of the characteristic eddy is very sensitive to the phases θ, so a compactness requirement can be used to determine the phases. This reasoning was employed by Herzog (1986). However, the compactness of a structure in space is difficult to define precisely. Instead, we consider some quantity of interest (e.g. one of the velocity components of the characteristic eddy) and determine the phases $\theta(k_x, k_z)$ to maximize the maximum value of its integral over y. Such a requirement leads to a structure that is compact in space. To see why this is so, let $I(x, z)$ be the integral of the quantity of interest in y. We define an integral area scale $\int I^2(x, z)\,\mathrm{d}x\,\mathrm{d}z/I^2(0, 0)$, which is a measure of the area in the x- and z-directions over which I is significantly non-zero. The integral in the numerator is independent of the phases of the Fourier coefficients of I, and is therefore independent of $\theta(k_z, k_z)$, if we consider quantities that are linear in the characteristic eddy velocity. Therefore, when the magnitude of $I(0, 0)$ is maximized, the area scale is minimized and the characteristic eddy is compact.

It is easy to show that this compactness condition is satisfied when the Fourier coefficients of the integral in y of the quantity of interest are real and positive for all wavenumbers. One could also define a compactness condition based on the value of a quantity of interest at a given y-location. The integral condition stated above is used to avoid the need to specify the y-location. In the results shown in §5, the compactness condition based on both the streamwise velocity u and the normal velocity v were used. In principle, the spanwise velocity w could also be used. However, the symmetries of $\boldsymbol{\Phi}_{ij}$ (see §§2 and 4.1), imply that for $k_z = 0$, either $\hat{\phi}_3$ or both $\hat{\phi}_1$ and $\hat{\phi}_2$ are identically zero. For all cases considered, $\hat{\phi}_3$ was zero so a compactness condition based on w would have left the phases of the $k_z = 0$ modes undetermined. For some higher eigenfunctions, it is $\hat{\phi}_1$ and $\hat{\phi}_2$ that are zero so a w compactness condition would be appropriate for them.

4.3. *Phase determination from wavenumber continuity*

Finally, we expect that if the wavenumbers are continuous, corresponding to an infinite domain in x and z, then $\hat{\phi}_i^c(k_x, k_z)$ will be a continuous function of the wavenumbers. Thus for the discrete wavenumbers in the computation, we expect that $\hat{\phi}_i^c(k_x, k_z)$ will not be very different for neighbouring wavenumbers. This expectation can be enforced to determine the phases $\theta(k_x, k_z)$. For ease of exposition, the procedure by which this is accomplished will be described for the two-dimensional (y and z) decomposition in which θ depends only on k_z. A similar though more complicated procedure is possible in three dimensions. The similarity of the eigenfunctions for neighbouring wavenumbers k_{zj} and k_{zj+1} results in the magnitude of the integral

$$\frac{\int \hat{\phi}_i^c(y, k_{zj})\, \hat{\phi}_i^{c*}(y, k_{zj+1})\,\mathrm{d}y}{[\lambda^{(1)}(k_{zj})\,\lambda^{(1)}(k_{zj+1})]^{\frac{1}{2}}} \tag{4.18}$$

being nearly unity. The phases $\theta(k_z)$ are set such that the integral (4.18) will be real and positive, which results in $\hat{\phi}_i^c$ for neighbouring wavenumbers being as parallel as possible. This procedure leaves an overall phase undetermined, which is set (except for an overall sign) by the requirement that $\hat{\phi}_i^c(k_z = 0)$ is real (i.e. $\theta(0) = 0$), which is necessary for ϕ_i^c to be real. The result of this specification of the phases will be called the zero-phase eddy because for all wavenumbers, the phases of $\hat{\phi}_i^c$ are the same in the sense just described.

4.4. *Overall algorithm*

A step-by-step description of the algorithm used to obtain the characteristic eddy given the two-point spectral-density tensor is presented here. These steps are those required to implement the u-compactness criteria, the other phase recovery techniques are similar.

(1) The matrix $\boldsymbol{A}$ (equation (3.9)) representing the numerical approximation of the integral in (4.1) is formed and symmetrized for each wavenumber.

(2) The eigenvalues and eigenvectors of $\boldsymbol{A}$ are obtained.

(3) For each wavenumber the eigenvector associated with the largest eigenvalue is selected.

(4) The eigenvector is scaled so that its energy (computed as $\int_D \hat{\phi}_i \hat{\phi}_i^* \, dy$, with the integral approximated by the trapezoidal rule) is equal to the associated eigenvalue.

(5) The eigenvector is multiplied by the complex quantity $\gamma^*/|\gamma|$, where $\gamma = \int_D \hat{\phi}_1 \, dy$. Again the integral is approximated using the trapezoidal rule.

(6) Once steps (1)–(5) are completed for each wavenumber, the eigenvectors are treated as the Fourier transform of a velocity field. The inverse Fourier transform in x and z is computed to obtain the physical-space representation of the eddy.

5. Characteristic eddies in multiple dimensions

In this section, the decomposition discussed in §§3 and 4 will be applied in both two and three dimensions. We consider the two-dimensional case separately because, as discussed in §4.1, we shall require the bispectrum, and only in the two-dimensional case do we have a sufficient statistical sample to obtain a reliable estimate of this quantity. In the two-dimensional case we wish to extract the dominant eddy as viewed in planes perpendicular to both the wall and the flow direction (y, z-planes). The relevant laboratory experiment would be to illuminate a (y, z)-plane with a light source in a smoke-filled channel flow and to identify characteristic eddies in this plane. For the two-dimensional case, (4.1) reduces to

$$\int_y \Phi_{ij}(y, y', k_z) \hat{\phi}_j^*(y', k_z) \, dy = \lambda(k_z) \hat{\phi}_i(y, k_z), \tag{5.1}$$

where the two-dimensional Φ_{ij} is the Fourier transform of R_{ij} (equation (2.1)) with $r_x = 0$. The eigenvalue problems (equations (4.1) and (5.1)) are solved numerically for each wavenumber using the method outlined in §3 (recall that the computation of the channel flow was done in a finite domain with a finite resolution so there are a finite number of discrete wavenumbers).

5.1. *Contributions to second-order moments*

The properties of the inhomogeneous decomposition developed in §3 can be extended immediately to the multiple-dimension case. In particular the contributions of the

Domain	Dimensions	$E^{(1)}/E$	$E^{(2)}/E$	$E^{(3)}/E$	$E^{(1)}/E^{(2)}$	$\Pi^{(1)}/P^{(t)}$
$0 \leqslant y^+ \leqslant 40$	2	0.64	0.17	0.07	3.8	1.05
$140 \leqslant y^+ \leqslant 180$	2	0.46	0.24	0.18	1.9	1.55
$0 \leqslant y^+ \leqslant 180$	2	0.38	0.16	0.09	2.3	0.77
$0 \leqslant y^+ \leqslant 40$	3	0.76	0.12	0.06	6.0	1.04
$140 \leqslant y^+ \leqslant 180$	3	0.57	0.22	0.12	2.5	1.53
$0 \leqslant y^+ \leqslant 180$	3	0.50	0.16	0.08	3.1	0.75

TABLE 2. Contributions of the two- and three-dimensional eigenfunctions to energy and production

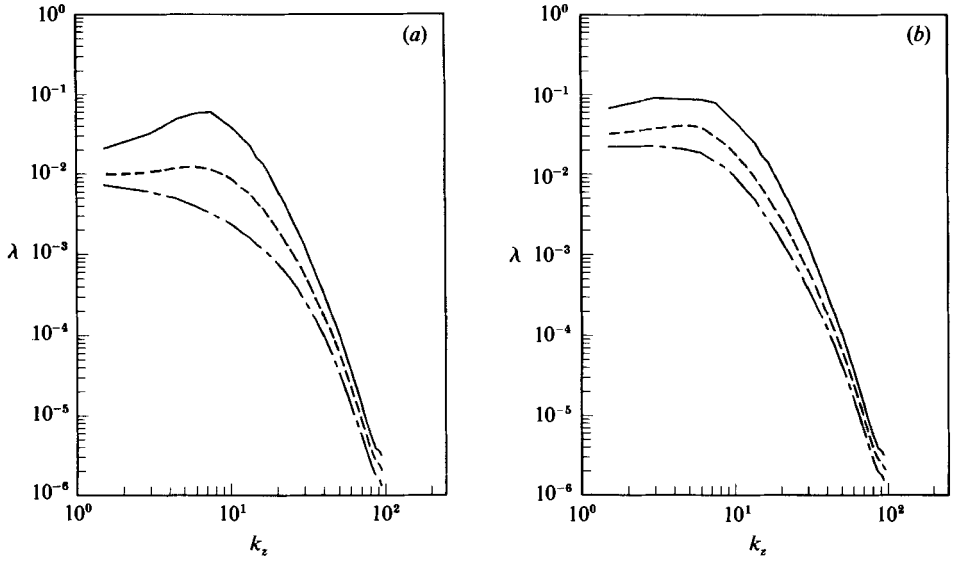

FIGURE 4. Eigenvalue spectra for the two-dimensional case, (*a*) near-wall domain and (*b*) wall-to-centreline domain: ——, first eigenvalue; --------, second eigenvalue; ———, third eigenvalue.

eigenfunctions to second-order statistics can be determined (independent of the phases):

$$\langle u_i u_j \rangle = \sum_n \langle u_i^{(n)} u_j^{(n)} \rangle = \sum_n \sum_{k_x} \sum_{k_z} \lambda^{(n)}(k_x, k_z)\, \phi_i^{(n)}(k_x, y, k_z)\, \phi_j^{(n)*}(k_x, y, k_z), \quad (5.2a)$$

and

$$E = \sum_n \sum_{k_x} \sum_{k_z} \lambda^{(n)}(k_x, k_z). \quad (5.2b)$$

For the two-dimensional case, the sums with respect to k_x and the dependence on k_x are not present. In table 2 the contribution of the first three characteristic eddies to turbulent kinetic energy ($E^{(n)} = \Sigma_{k_x, k_z} \lambda^{(n)}(k_x, k_z)$) are shown for the same domains as in §3, for both two- and three-dimensional cases. Again, as an indicator of the contribution of the dominant eddy to turbulence production the quantity $\Pi^{(1)}/P^{(t)}$ is also tabulated, where

$$\Pi^{(1)} = \sum_{k_x} \sum_{k_z} \int_{y_l}^{y_u} \lambda^{(1)}(k_x, k_z)\, \hat{\phi}_1^{(1)}(k_x, y, k_z)\, \hat{\phi}_2^{(1)*}(k_x, y, k_z)\, \mathrm{d}y \quad (5.3)$$

and $P^{(t)}$ is defined in §3.

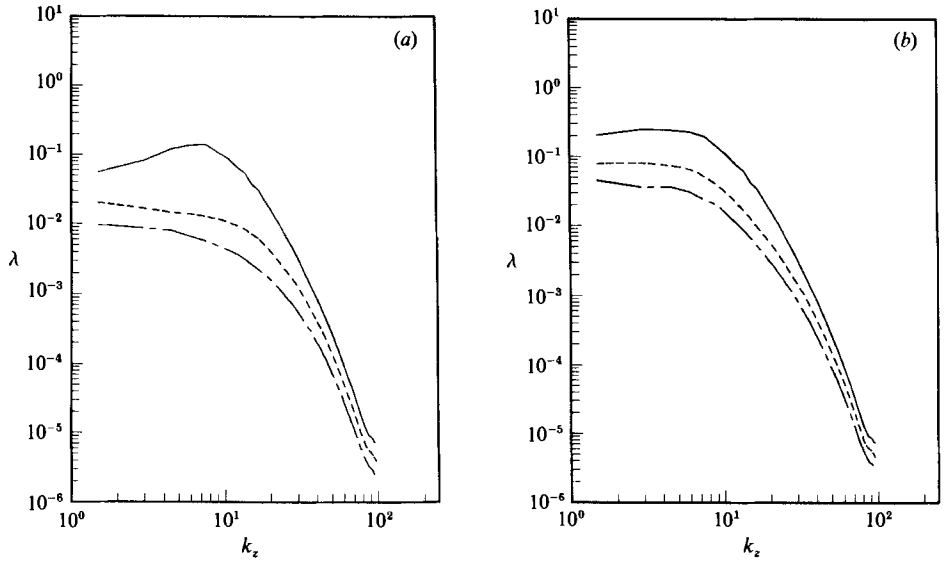

FIGURE 5. Eigenvalue z-spectra for the three-dimensional case, (a) near-wall domain and (b) wall-to-centreline domain: ——, first eigenvalue; - - - - - - - -, second eigenvalue; — — —, third eigenvalue.

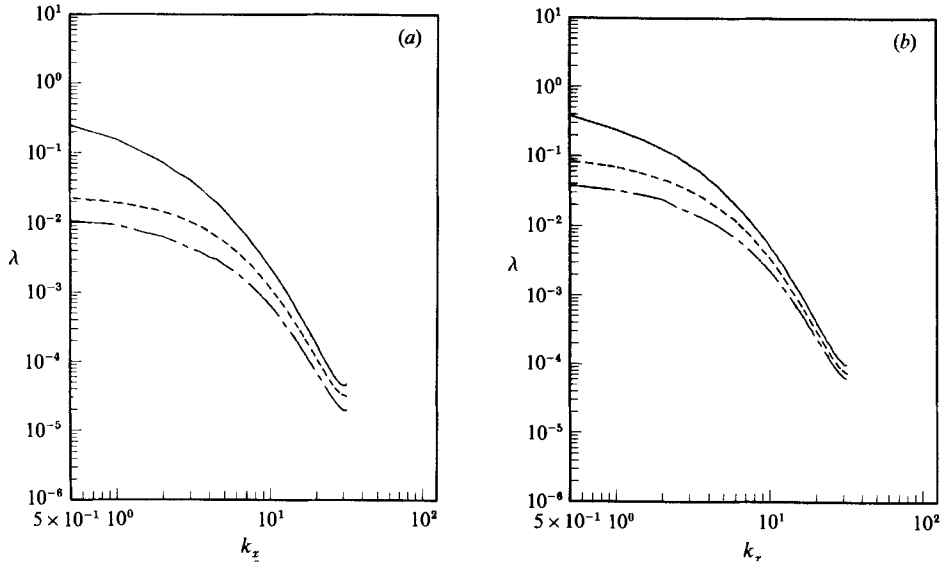

FIGURE 6. Eigenvalue x-spectra for the three-dimensional case, (a) near-wall domain and (b) wall-to-centreline domain: ——, first eigenvalue; - - - - - - - -, second eigenvalue; — — —, third eigenvalue.

As in the one-dimensional case the dominant eddy makes a significant contribution to turbulence kinetic energy and production. The contribution of the dominant eddy to turbulent kinetic energy is somewhat higher than in the one-dimensional case, and is higher in three dimensions than in two dimensions. Note also that, as in the one-dimensional case, the energy contribution of the dominant eddy is much greater for the near-wall domain than for the same size domain at the centre of the channel. This

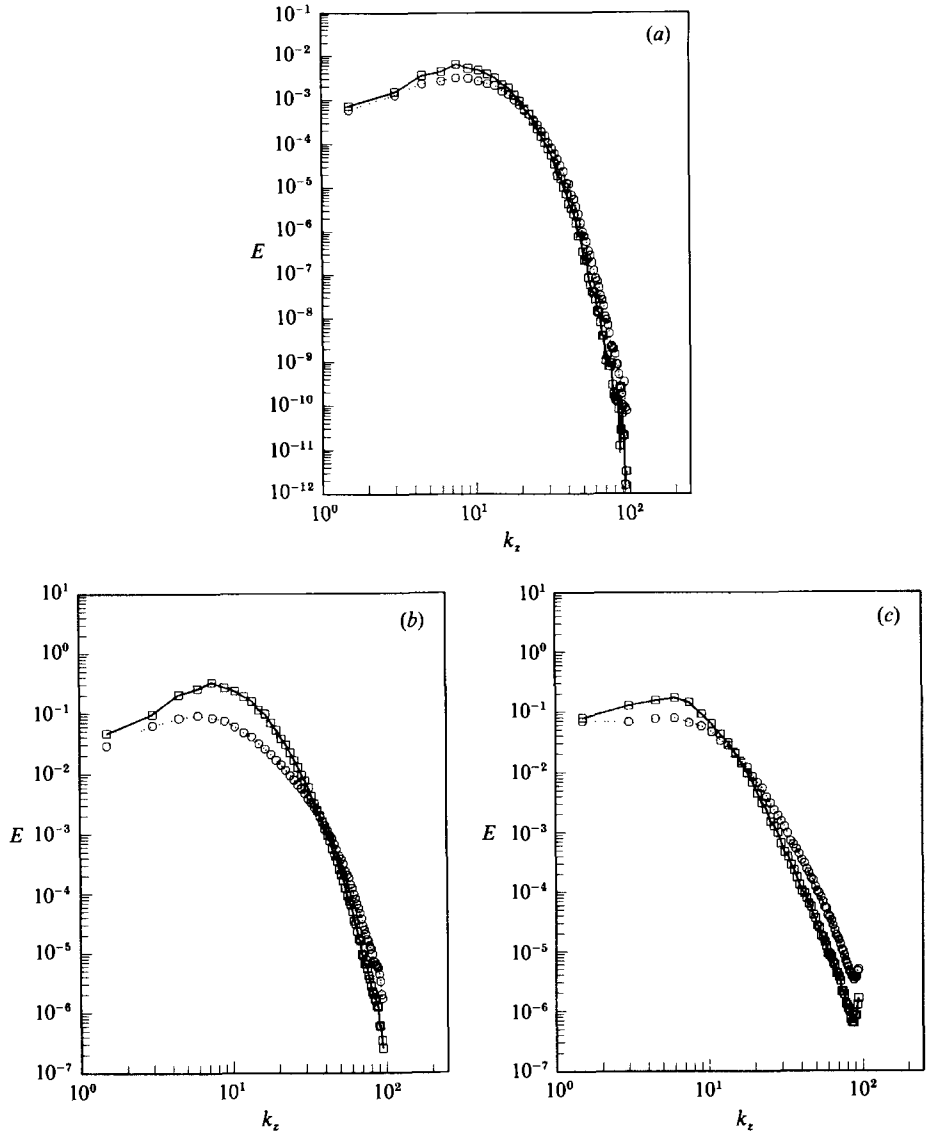

FIGURE 7. Contributions to the z-energy spectrum of the first eigenfunction (□), and second eigenfunction (○) at (*a*) $y^+ = 1.5$, (*b*) $y^+ = 10$ and (*c*) $y^+ = 40$ for the two-dimensional case in the near-wall domain ($y^+ \leqslant 40$).

again suggests that the near-wall turbulence is more organized than that away from the wall.

The spectra of the first three eigenvalues for the wall layer ($y^+ \leqslant 40$) and the domain extending from the wall to the centreline are shown in figure 4 for the two-dimensional case and figures 5 and 6 for the three-dimensional case. In both two and three dimensions, the z-spectrum of the dominant eigenvalue in the wall layer shows a pronounced peak at the non-dimensional wavenumber $k_z\delta = 7.5$, which corresponds to the wavelength $\lambda_z^+ = 150$. The higher-order eigenvalues have no such peak, and do not show a shift to higher k_z values as would have been expected if small

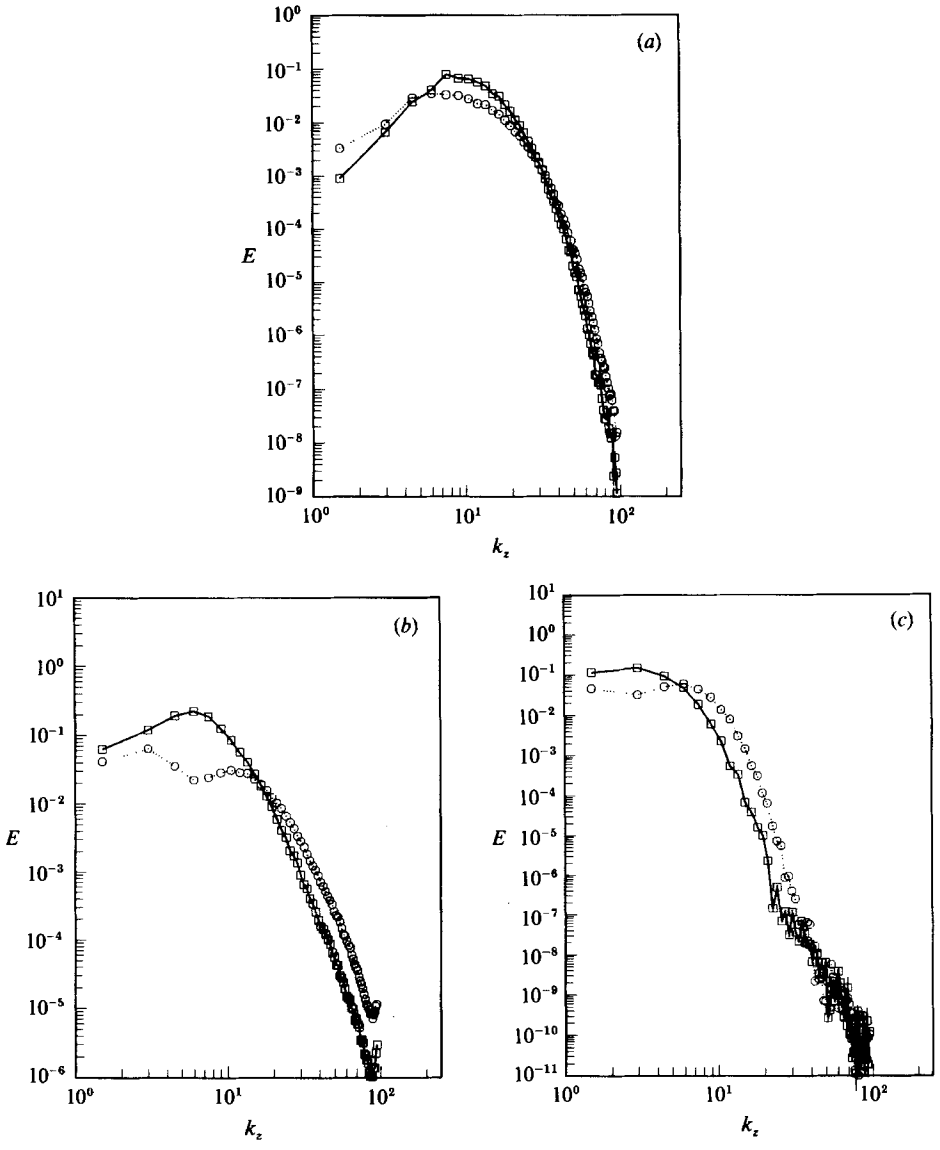

FIGURE 8. Contributions to the z-energy spectrum of the first eigenfunction (□), and second eigenfunction (○) at (*a*) $y^+ = 5.4$, (*b*) $y^+ = 40$ and (*c*) $y^+ = 91$ for the two-dimensional case in the wall-to-centreline domain ($y^+ \leqslant 180$).

vertical scales were associated with small horizontal scales. The x-spectra for the three-dimensional case fall off monotonically, similar to the streamwise turbulent kinetic energy spectra (see Kim *et al.* 1987).

For the two-dimensional case, the contributions of the first two eigenfunctions to turbulent kinetic energy spectra,

$$E^{(n)}(k_z, y) = \hat{f}_i^{(n)}(k_z, y)\hat{f}_i^{(n)*}(k_z, y) = \lambda^{(n)}(k_z)\,\hat{\phi}_i^{(n)}(y, k_z)\,\hat{\phi}_i^{(n)*}(y, k_z), \tag{5.4}$$

at selected y-locations are shown in figures 7 and 8 for the near-wall and the wall-to-centreline domains respectively. At most y-locations the contribution of the dominant eddy is larger than the second eigenfunction at low wavenumbers and

smaller at high wavenumbers. An exception is shown in figure 8(*a*) where the second characteristic eddy is in fact more energetic than the dominant eddy at the lowest wavenumbers. The higher-order eigenfunctions are associated with smaller scales in the y-direction but not necessarily with smaller scale motions in the z-direction. Note that the decomposition theorem requires that at any wavenumber the integral of $E^{(1)}$ over y be larger than that of $E^{(2)}$. These integrals are of course equal to respective eigenvalues plotted in figure 4.

The spectra of the dominant eigenfunctions are broadbanded, but as expected are confined to a narrower range of energetic wavenumbers than the velocity spectra (see Kim *et al.* 1987). Fourier decomposition of structures confined to a finite region in space leads to broadband spectra such as those shown in figures 7 and 8. Spectra with very pronounced peaks result from distinct Fourier modes which, in contrast to compact eddies, extend indefinitely in space.

The spectra in figures 7(*c*) and 8(*b*) turn up slightly at high wavenumbers, while the spectra in figure 8(*c*) are very noisy at high wavenumbers. The noise in figure 8(*c*) is caused by round-off error. The data used in these decompositions was stored with seven digit accuracy, thus when spectra fall off by more than six or seven orders of magnitude, noise as in figure 8(*c*) is expected. The up-turns in figures 7(*c*) and 8(*b*) are caused by the finite resolution of the simulations. In the simulations, the dynamics of the highest wavenumbers are not well represented because of the presence of the resolution cut-off. These anomalies in the spectra should have little or no affect on the simulations or the decompositions since they represent an insignificant amount of energy.

5.2. *Characteristic eddies in the* (y, z)*-plane*

We now turn to the problem of finding the two-dimensional characteristic eddy ϕ_i^c. The magnitudes of the Fourier coefficients of f, as defined in (4.7), are found from (4.10), which in two dimensions reduces to

$$|\hat{f}(k_z)| = [\lambda^{(1)}(k_z)]^{\frac{1}{2}}. \tag{5.5}$$

To obtain the phases of $\hat{f}$, we consider the three techniques discussed in §4: the bispectrum, compactness and continuity in wavenumber space (zero-phase eddy).

The bispectrum of a_1 (a real quantity) is plotted in figure 9(*a*) for the near-wall domain, the bispectra for the other domains are similar. In all three domains the bispectrum is positive over almost the entire wavenumber domain, there are only small negative regions along the axes where either k_z, k_z' or $k_z + k_z'$ is zero. Because the bispectrum of a_1 is positive almost everywhere, the solution to the least-squares problem discussed in §4.1 is not significantly different from the zero-phase eddy on which the sign of B_{a_1} is based. In fact there is only a difference between the zero-phase eddy and the bispectrum-derived eddy for the near-wall domain ($0 \leqslant y^+ \leqslant 40$), and it turns out that the difference is at only one wavenumber. With f defined by the approximate solution of (4.13), the bispectrum of g can be computed, and is shown in figure 9(*b*) for the near-wall domain. In all three cases, the bispectrum is again positive almost everywhere, as we require.

Two compactness conditions have been used to determine the phases of $\hat{f}$. They require that for $i = 1$ and 2 the integrals $\int \phi_i^c(y, z)\,dy$ obtain their maximum possible value somewhere in the domain; in particular we choose that they be maximized at $z = 0$. These are the u- and v-compactness conditions respectively. It is interesting that for the two domains including the wall ($y^+ < 40$ and $y^+ < 180$), the u compactness condition is satisfied by the zero-phase eddy, though the v-compactness

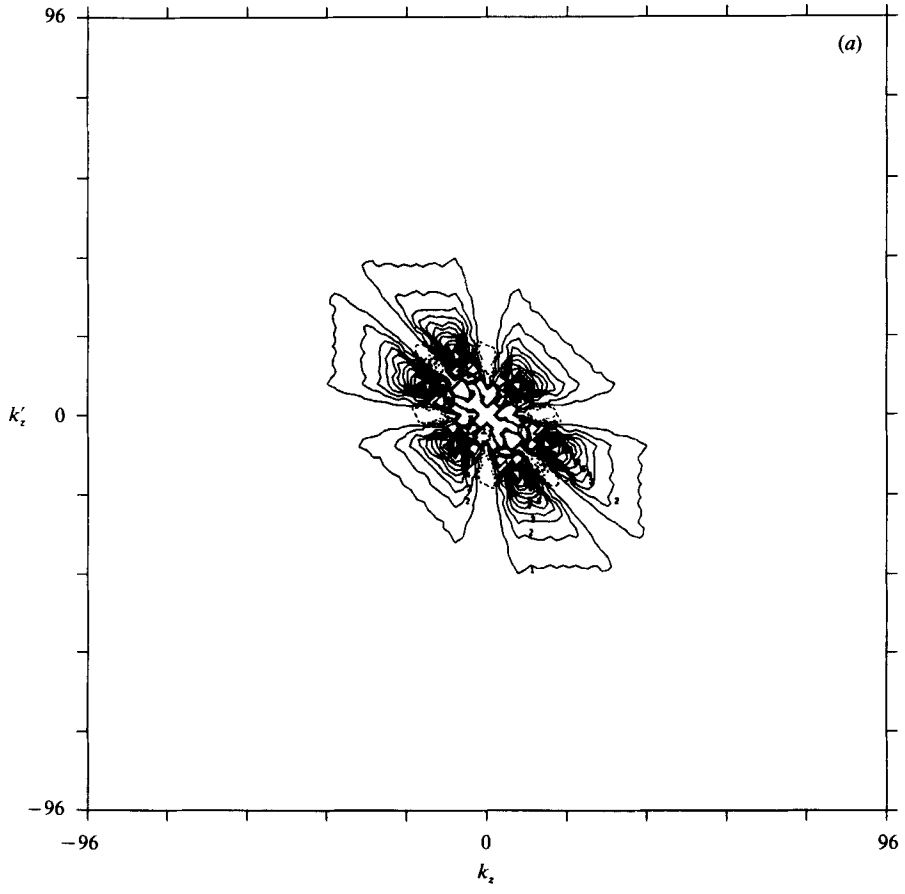

FIGURE 9(a). For caption see facing page.

condition is not. In the other domain ($140 \leqslant y^+ \leqslant 180$) the v-compactness condition but not the u-condition is satisfied by the zero-phase eddy. Note, that the w-compactness condition is not considered, as discussed in §4.2.

We now turn to the structure of the characteristic eddies in two dimensions. Figures 10 and 11 show the characteristic eddies with phases determined from the zero-phase condition. In the wall domain ($y^+ < 40$) the characteristic eddy consists of a narrow intense region of low streamwise velocity, which is about 50 wall units wide. There is also a very narrow (25 wall units) region of intense velocity away from the wall. The velocity vectors projected into the (y, z)-plane show that at the top of the domain there is a weak flow away from the centre of the jet, making a vortex.

In the wall-to-centreline domain ($y^+ < 180$) the characteristic eddy consists of low streamwise velocity with normal velocity away from the wall, similar to that in the near-wall domain. Near the wall the widths of these regions are the same as in the wall domain. Away from the wall, these regions become diffuse. Near the wall, the velocity vectors reveal a pattern similar to the near-wall domain, although the centre of the circulation region is somewhat higher than in the near-wall domain.

In both the near-wall domain ($y^+ \leqslant 40$) and the wall-to-centreline domain, the characteristic eddy consists of an ejection and the accompanying low-speed region.

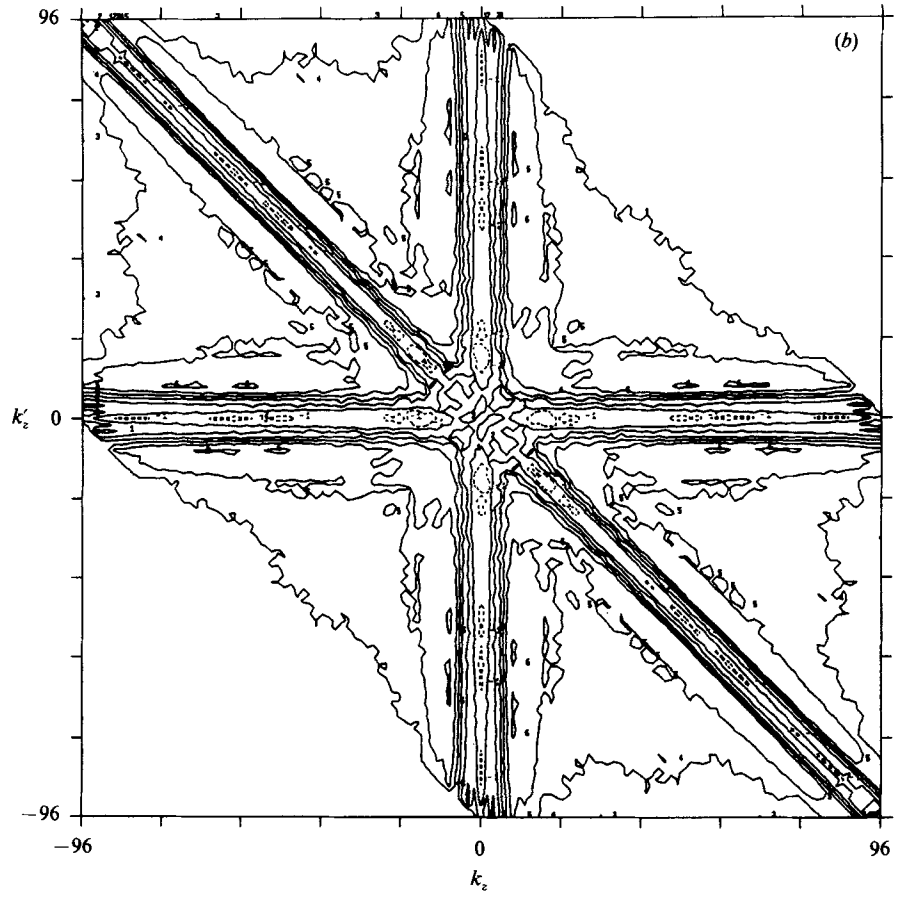

FIGURE 9. Contours of the bispectrum of (*a*) the process a_1 (see (4.3)), and (*b*) the process g (see (4.6)) in the near-wall domain ($y^+ \leqslant 40$). k_z and k_z' are zero in the centre of the plot. Dashed contours are negative. Contour increment is (*a*) 10^{-4}, (*b*) 0.05. Note the twelve-fold symmetry of the bispectrum function.

If the sign of ϕ_i^c were reversed the eddy would represent high-speed fluid moving towards the wall (sweep). The overall sign of the eddies is chosen for consistency with the bispectrum-derived eddy since the compactness conditions and the zero-phase condition leave the overall sign undetermined. The results of quadrant analysis in this flow indicate that ejections should be dominant far from the wall while sweeps are dominant near the wall (Wallace, Eckelmann & Brodkey 1972). Quadrant analysis indicates that the cross-over point for the dominance of sweeps and ejections is at $y^+ \approx 12$–15. The sign of the eddy is determined from third-order statistics, which also indicate the change in dominance from sweeps to ejections. In particular, the skewness of u goes from positive to negative at $y^+ \approx 15$ (Kim *et al.* 1987). Thus, even in the near-wall domain ($y^+ \leqslant 40$), ejections are dominant for a majority of the domain, explaining the ejection characteristic eddy in the near-wall domain. To test these arguments, the characteristic eddy was computed in the domain $y^+ \leqslant 10$. The resulting eddy represented sweep motion as expected.

Another interesting aspect of these characteristic eddies is that the magnitudes of the velocities are quite large. For example, in the near-wall domain the maximum (most negative) u-velocity is -16 (normalized by u_τ) as compared to the maximum

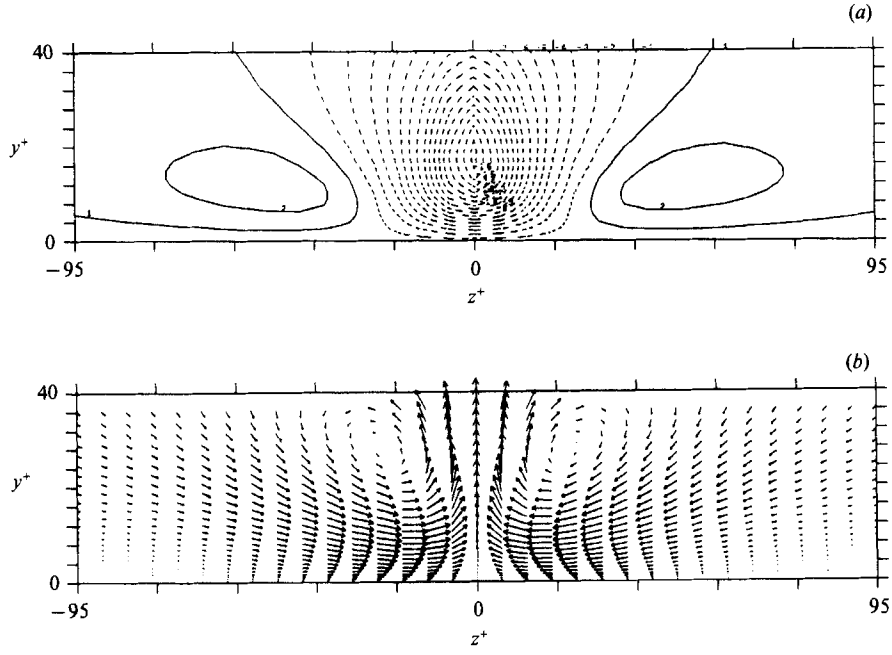

FIGURE 10. Two-dimensional zero-phase characteristic eddy in the near-wall domain ($y^+ \leqslant 40$), (*a*) contours of u and (*b*) velocity vectors projected into the (y, z)-plane. Contour increment in (*a*) is 1. Negative contours are dashed.

r.m.s. value of about 2.7. Note that the integral of the characteristic-eddy velocity over z is a substantial fraction of the r.m.s. velocity fluctuation, and the characteristic eddy is confined to a relatively small region, resulting in the large local velocities observed.

The characteristic eddies just considered satisfied one of the two compactness conditions discussed above (the u-condition) as well as the zero-phase condition. Characteristic eddies satisfying the v-compactness condition and the bispectrum condition have also been generated and are nearly indistinguishable from figures 10 and 11. The main difference is that the maximum value attained by u is slightly smaller (9% in the near-wall domain) and the maximum value attained by v is slightly larger (6% in the near-wall domain). The reason for this similarity is that the differences between the criteria are either in the higher wavenumbers ($k_z > 50$) where the spectrum has already fallen off significantly (see figure 4), or there is a difference at only one or two wavenumbers.

To evaluate the extent to which the characteristic eddy is observable, an instantaneous velocity field has been examined for structures. To find the locations of events corresponding to the characteristic eddy, sample functions of $g(z)$ have been computed for the near-wall domain from the sample functions of a_1 using (4.7*b*). An example obtained at a particular x and time is given in figure 12(*a*), which shows a large isolated positive excursion of g from zero at about $z = 3.1\delta$. This should correspond to a structure similar to the characteristic eddy. A vector plot of the velocity in the (y, z)-plane centred at this location is shown in figure 12(*b*) for comparison with figure 10(*b*). As in the characteristic eddy, there is a large streamwise vortex to the left of the domain, with a flow away from the wall at the centre of the domain. The shape of this vortex is somewhat different from the

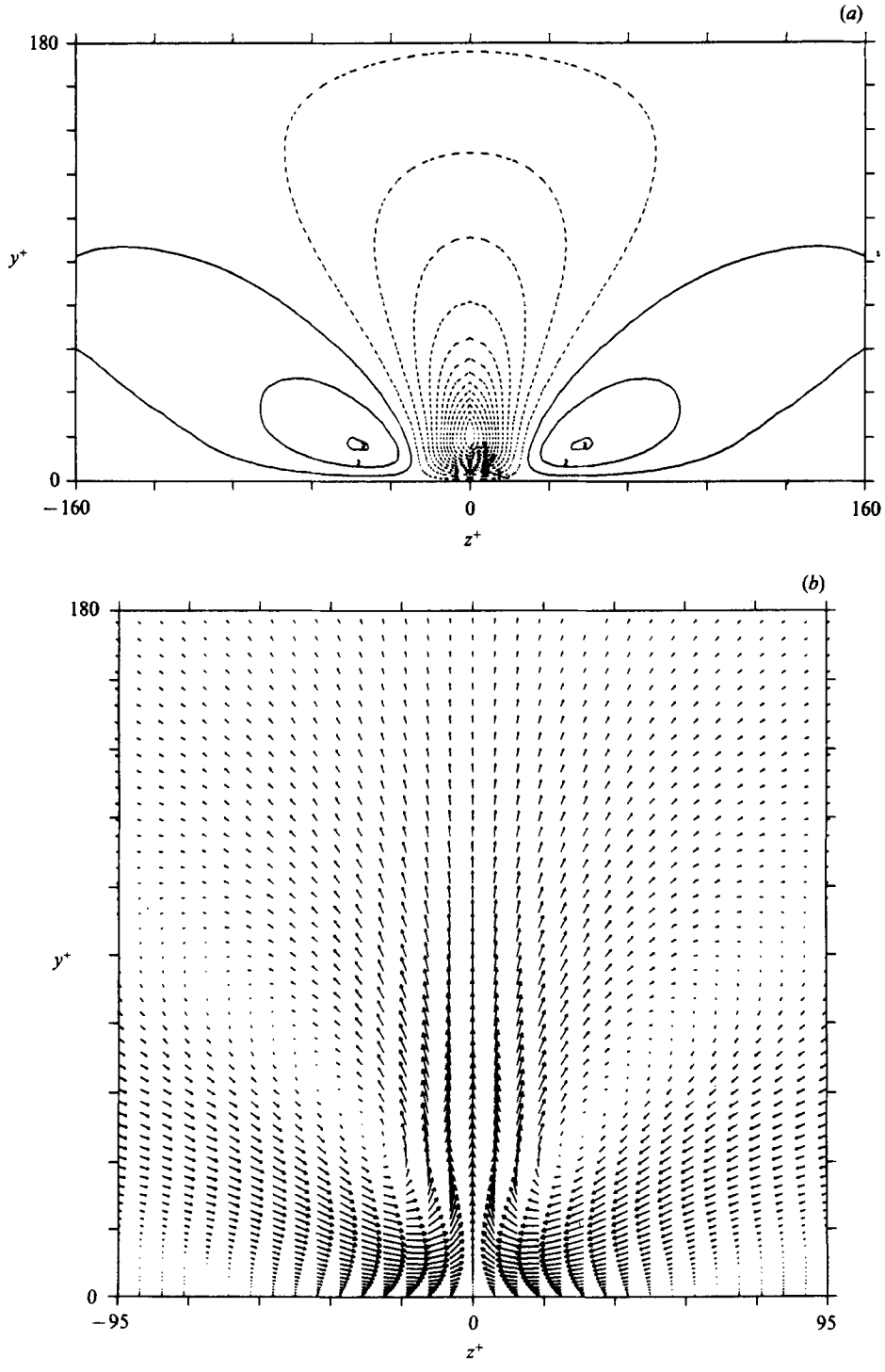

FIGURE 11. Two-dimensional zero-phase characteristic eddy in the wall-to-centreline domain ($y^+ \leqslant 180$), (*a*) contours of u and (*b*) velocity vectors projected into the (y, z)-plane. Contour increment in (*a*) is 1. Negative contours are dashed.

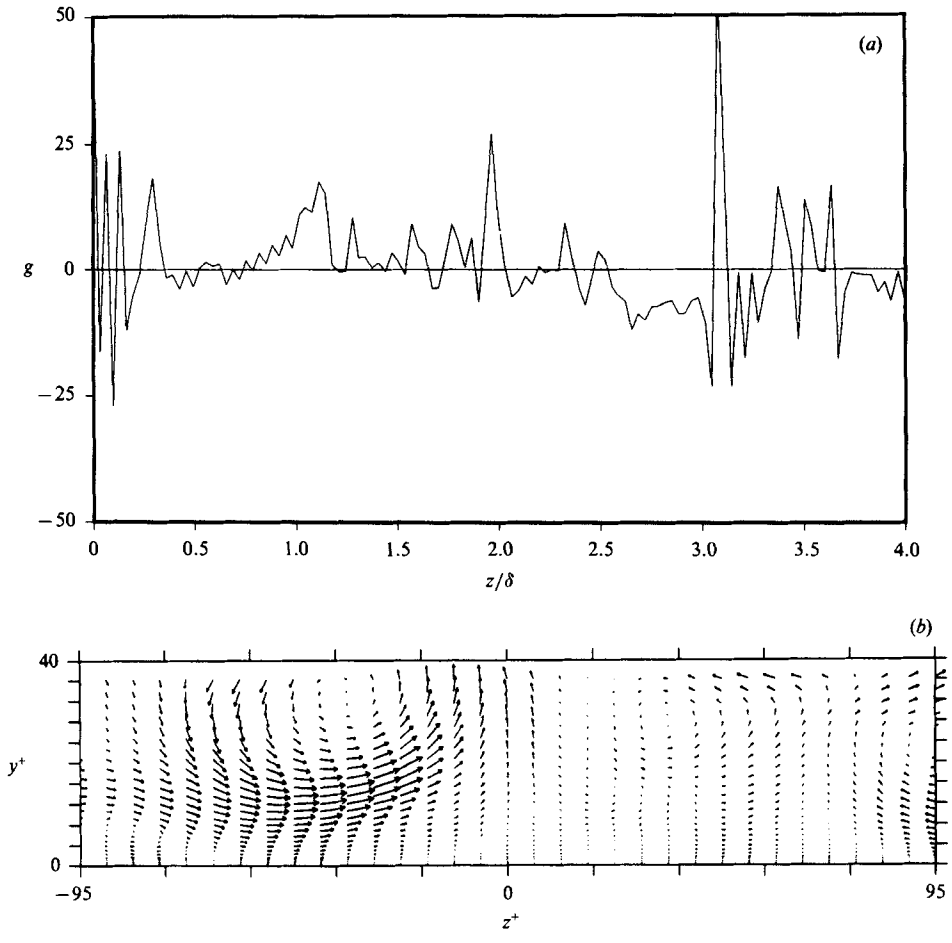

FIGURE 12. (*a*) Sample functions of the g-process (see (4.8)) from the two-dimensional decomposition in the near-wall domain. (*b*) Velocity vectors projected into the (y, z)-plane of the instantaneous velocity in the plane from which the sample function of g shown in (*a*) was taken. The plot domain is centred on the large peak in g appearing at $z = 3.1\delta$.

vortices in the characteristic eddy. The major difference between the instantaneous structure and the characteristic eddy is the lack of a counter-rotating partner in the instantaneous field. It is important to note that the appearance of counter-rotating *pairs* of vortices in the characteristic eddy is a consequence of the symmetries in the statistics and the techniques by which the phases were determined, and does not imply that such pairs are prevalent in the instantaneous fields. Thus, the major difference in this case is due to this 'artificial' symmetry imposed on the characteristic eddy (see §6 for further discussion of this point).

5.3. *Characteristic eddies in three dimensions*

In three dimensions we must determine the function $f(x, z)$ as defined in (4.7). When g satisfies (4.8), the magnitude of the Fourier coefficients of f are

$$|\hat{f}(k_x, k_z)| = [\lambda^{(1)}(k_x, k_z)]^{\frac{1}{2}}. \tag{5.6}$$

The phases of $\hat{f}$ were determined by the compactness conditions discussed in §4 and

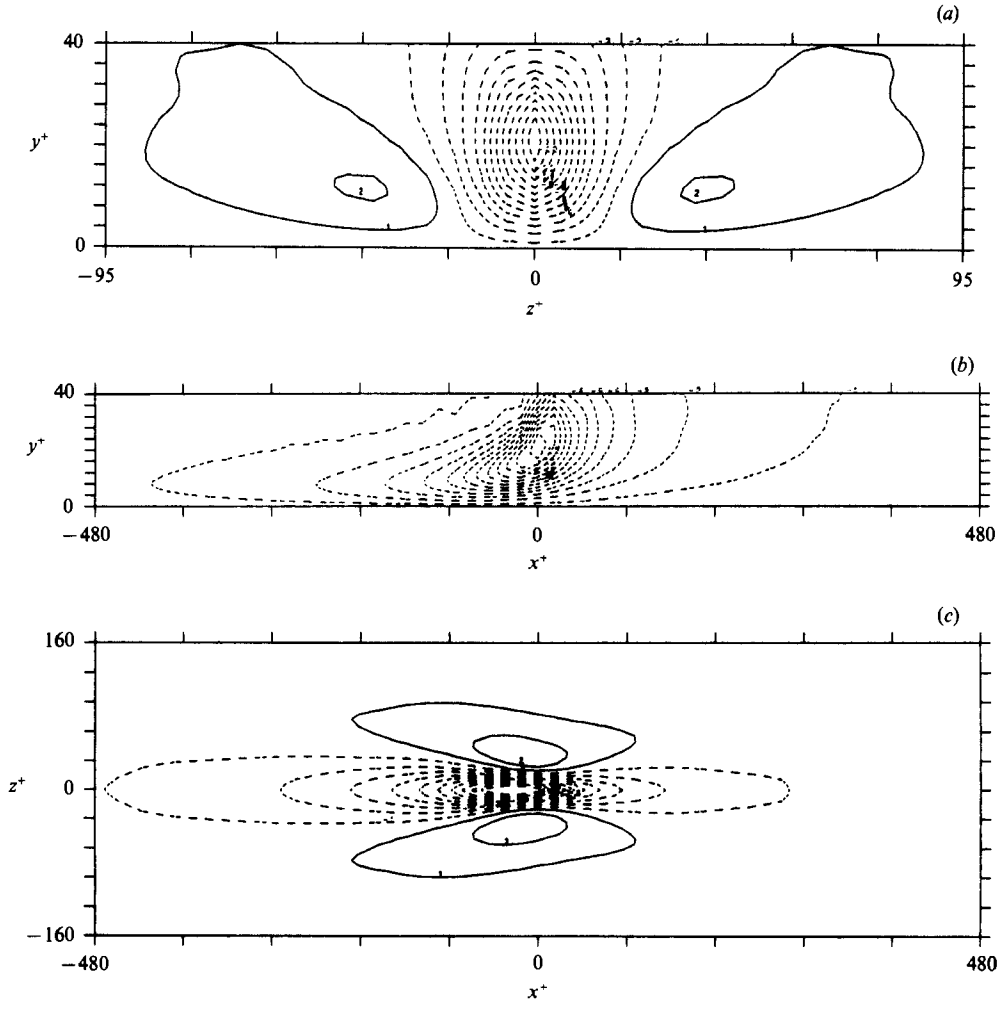

FIGURE 13. Contours of ϕ_1^c for the three-dimensional zero-phase characteristic eddy in the near-wall domain ($y^+ \leqslant 40$). (*a*) (y,z)-plane at $x = 0$, (*b*) (x,y)-plane at $z = 0$, (*c*) (x,z)-plane at $y^+ = 10$. Contour increment is (*a*) 7, (*b*) 7, (*c*) 5. Negative contours are dashed.

the zero-phase condition. The bispectrum is not used in the three-dimensional case because the statistical sample available did not allow it to be accurately estimated. In the two-dimensional case the compactness and bispectrum conditions produce the same results, but it is not clear that this would occur in three dimensions.

In addition to the zero-phase condition, the phases of $\hat{f}$ have been chosen to make the maximum values attained by $\int \phi_i^c(x,y,z)\,\mathrm{d}y$ as large as possible for $i = 1$ or $i = 2$, resulting in u- and v-compactness conditions. Unlike the two-dimensional case, the zero-phase characteristic eddy does not satisfy either of these compactness conditions. There is very little difference in the structure of the characteristic eddy between the two compactness criteria for the near-wall domain, but the magnitude of the maximum values of the velocities do differ. There are some discernible differences between the zero-phase eddy and the eddies derived from the compactness criteria in the wall-to-centreline domain; these differences are also discussed below.

Contours of the streamwise and normal velocity components for the zero-phase

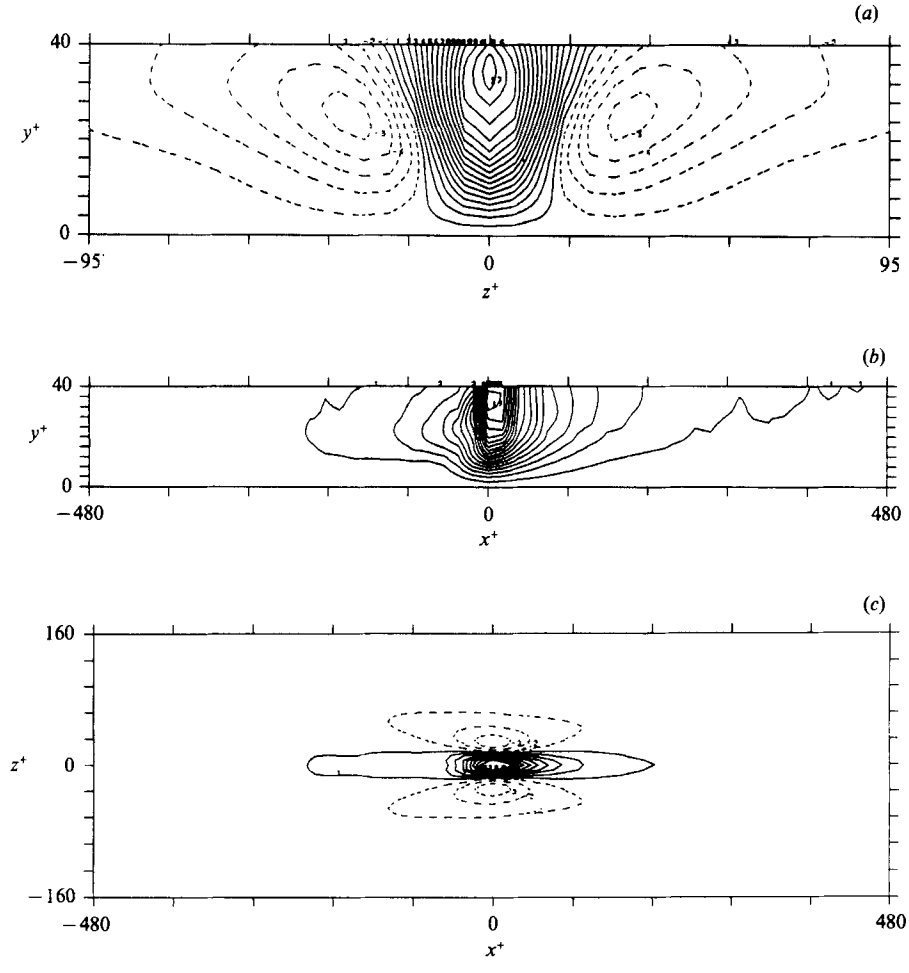

FIGURE 14. Contours of ϕ_2^c for the three-dimensional zero-phase characteristic eddy in the near-wall domain ($y^+ \leqslant 40$). (*a*) (y,z)-plane at $x = 0$, (*b*) (x,y)-plane at $z = 0$, (*c*) (x,z)-plane at $y^+ = 10$. Contour increment is (*a*) 1, (*b*) 1, (*c*) 0.6. Negative contours are dashed.

eddy are shown in figures 13 and 14 for the near-wall ($y^+ < 40$) domain. Shown are contours in the (y,z)-plane at $x = 0$, the (x,y)-plane at $z = 0$ and the (x,z)-plane at $y^+ \approx 10$. The location $x = 0, z = 0$ is where both the streamwise and normal velocities attain their maximum values, and can therefore be regarded as the centre of the eddy. In the near-wall domain the (y,z)-contours reveal a region of low streamwise velocity approximately 50 wall units wide and coincident with a region of strong velocity away from the wall. This is consistent with the two-dimensional results. The (x,y)-contours show that the low streamwise velocity region extends 250 wall units upstream of $x = 0$ near the wall, decreasing to as little as 60 wall units upstream at $y^+ = 40$. In contrast, the downstream extent of the low velocity region (150 wall units) does not decrease away from the wall. The region of intense vertical velocity has a streamwise extent of less than 100 wall units in the upstream and downstream directions. This is also evident in the (x,z)-contours in the plane at $y^+ = 10$.

Contours for the u-compactness condition characteristic eddy in the wall-to-centreline domain are shown in figures 15 and 16. The v-compactness condition plots

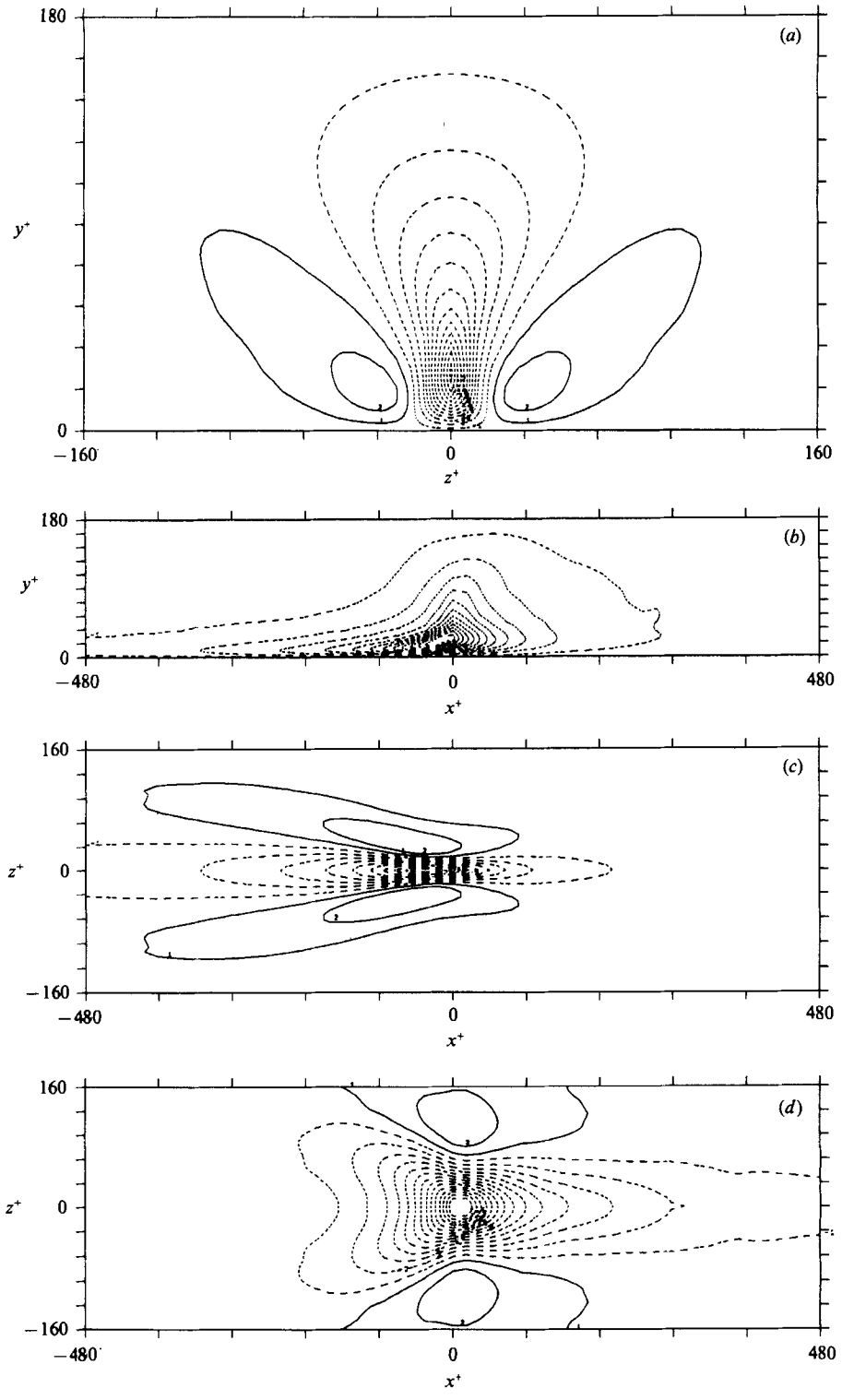

FIGURE 15. Contours of ϕ_1^c for the three-dimensional u-compactness characteristic eddy in the wall-to-centreline domain ($y^+ \leqslant 180$). (*a*) (y,z)-plane at $x = 0$, (*b*) (x,y)-plane at $z = 0$, (*c*) (x,z)-plane at $y^+ = 10$, (*d*) (x,z)-plane at $y^+ = 95$. Contour increment is (*a–c*) 5, (*d*) 1. Negative contours are dashed.

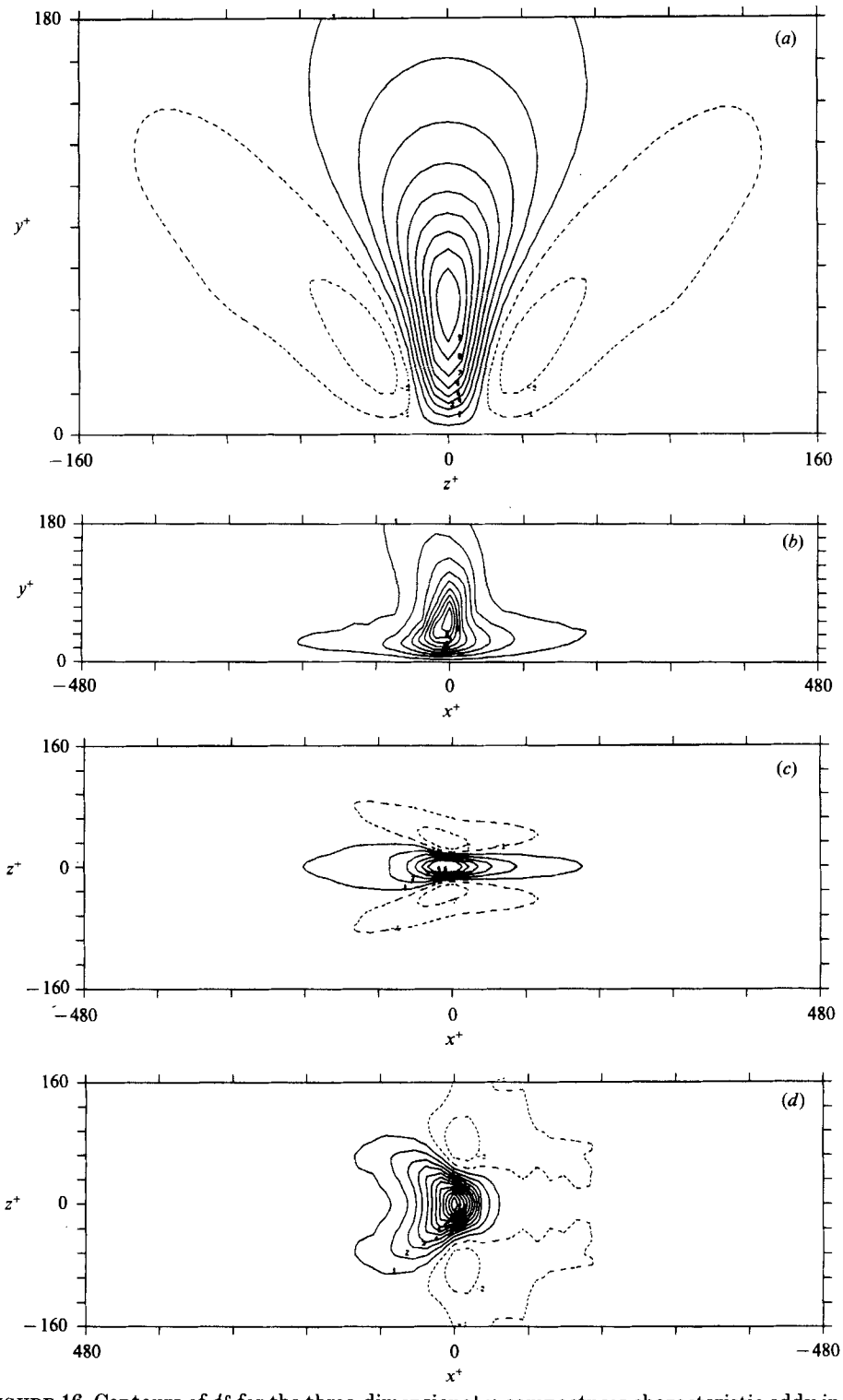

FIGURE 16. Contours of ϕ_2^c for the three-dimensional u-compactness characteristic eddy in the wall-to-centreline domain ($y^+ \leqslant 180$). (*a*) (y,z)-plane at $x = 0$, (*b*) (x,y)-plane at $z = 0$, (*c*) (x,z)-plane at $y^+ = 10$, (*d*) (x,z)-plane at $y^+ = 95$. Contour increment is (*a–c*) 2, (*d*) 0.9. Negative contours are dashed.

are similar, except for the magnitudes of the velocities. As in the two-dimensional case, the near-wall region of the characteristic eddy in the wall-to-centreline domain is remarkably similar to that in the near-wall domain. Contours in the (y, z)-plane in figures 15 and 16 indicate that the region of low streamwise velocity and flow away from the wall are diffuse far from the wall, having a z extent as much as three times that near the wall. However, in the (x, y)-plane, it is seen that these regions have smaller streamwise extents far from the wall than near the wall. Far from the wall, the low streamwise velocity region has an extent of about 100 wall units, as does the region of high vertical velocity. Contours of u and v in the (x, z)-plane at $y^+ = 95$ reveal that, upstream of $x = 0$, the highest values of u and v occur off the $z = 0$ axis. This is related to the pair of streamwise vortices in the characteristic eddy, since above these vortices, the maximum normal velocity does not occur on the midplane between them, but to the sides. The zero-phase characteristic eddy has also been computed; the major difference between it and the u-compactness eddy in figures 15 and 16 is the vertical location of the streamwise vortices (see below).

Figure 17 contains plots of the velocity vectors projected into (y, z)-planes located at $x^+ = 0, \pm 18$ and ± 36 for the zero-phase eddy in the *near-wall domain*. The plane at $x = 0$ reveals a pair of counter-rotating vortices straddling the region of strong ejection from the wall. In the wall-to-centreline domain, a similar set of streamwise vortices occur (not shown). The centres of the vortices in the near-wall domain at $x = 0$ are located at $y^+ = 25$ and are separated by 35 wall units. Upstream of $x = 0$, the centres are closer to the wall, and downstream, they are farther away. At $x^+ = 36$, the centres are beyond the edge of the domain. The y-location of the vortex centres is plotted in figure 18. Note that the angle of inclination of the vortex increases with downstream location. At $x^+ = -36$ the angle is 10° while at $x^+ = 18$, the angle is 31°. Upstream of $x^+ = -54$ (plots not shown), the vortices are so weak that they are not discernible. Thus, in the wall region ($y^+ < 40$), the vortices have a streamwise extent of less than 100 wall units. This is consistent with the observations of streamwise vortices in instantaneous velocity fields made by Moser & Moin (1984), in which the vortices were observed to go beyond $y^+ = 40$ in a very short streamwise distance (150 wall units). In contrast, the streamwise vortices in the decomposition performed by Herzog (1986) were near the wall for a much longer streamwise distance (360 wall units), and had a nearly constant angle of inclination of 5°. The reason for this discrepancy is not known, but the poor streamwise resolution of Herzog's measured correlation tensor for moderate to large separations (see §1) is a potential cause.

Moser & Moin (1984) observed that there were many more solitary vortices than vortex pairs in instantaneous flow fields. It may appear that there is a contradiction between the counter-rotating pair of vortices obtained by the decomposition and this prevalence of solitary vortices observed in instantaneous velocity fields. This is not the case. The technique outlined in §§3 and 4 yields symmetric counter-rotating pairs of vortices, which are distributed through the homogeneous spatial directions by the sprinkling process g (see (4.6)). As was observed in figure 12, there is no difficulty in generating a solitary vortex from a collection of vortex pairs when they are distributed by the appropriate g-function. The fact that vortices are obtained by the current method indicates the importance (as measured by energy) of these vortices near the wall. The fact that a pair of vortices is obtained rather than a solitary vortex calls for improvement in the phase recovery technique.

Also shown in figure 18 are the vortex-centre positions for the characteristic eddies in the near-wall domain based on the u and v compactness conditions, as well as

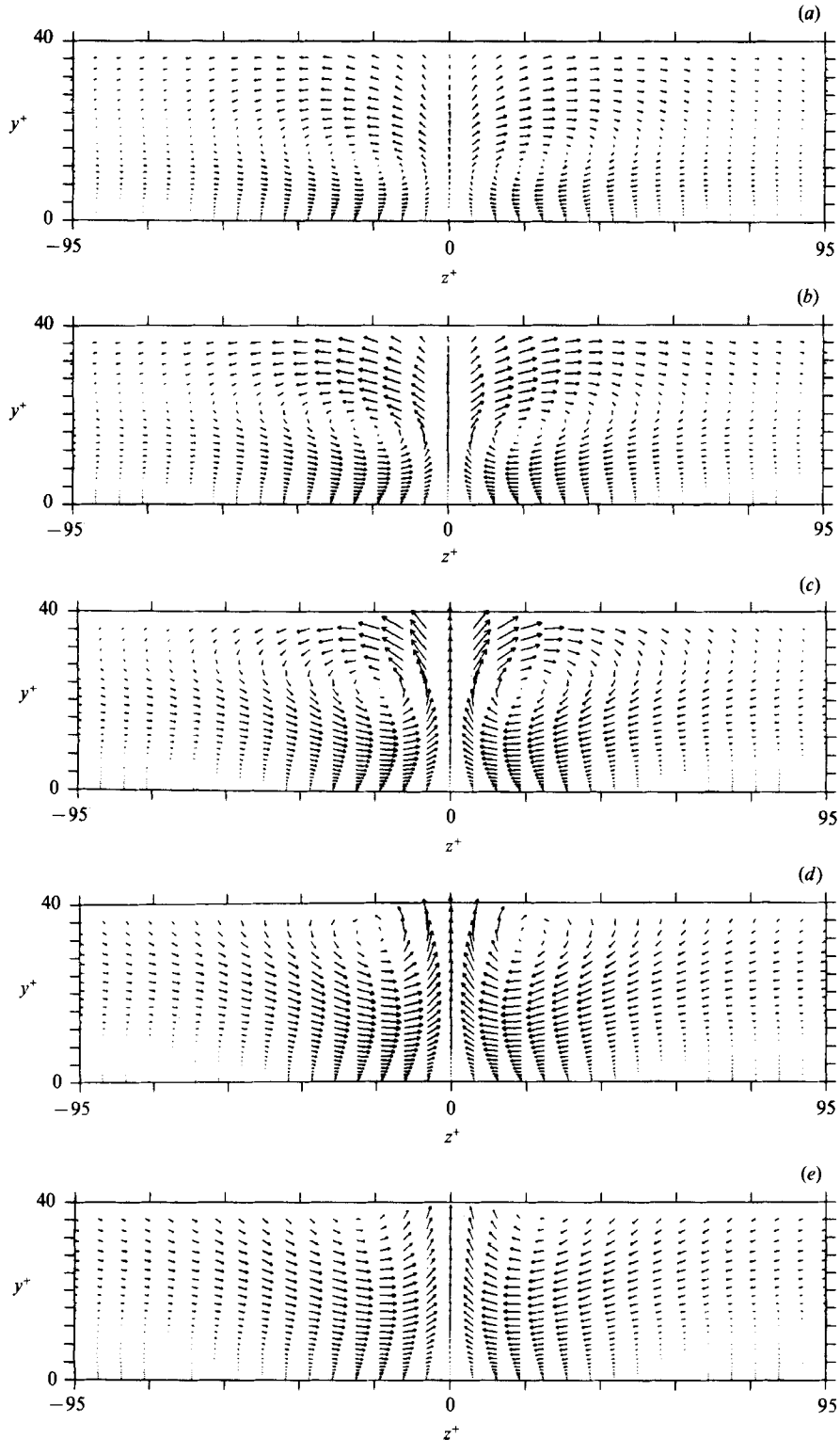

FIGURE 17. Velocity vectors for the zero-phase eddy in the near-wall domain ($y^+ \leqslant 40$) projected into (y, z)-planes at (*a*) $x^+ = -36$, (*b*) $x^+ = -18$, (*c*) $x^+ = 0$, (*d*) $x^+ = 18$ and (*e*) $x^+ = 36$.

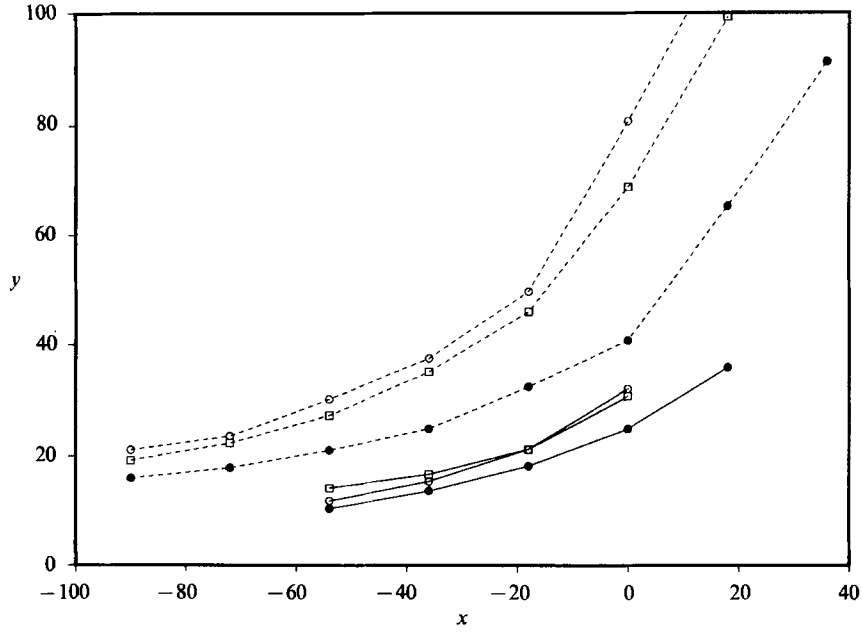

FIGURE 18. Vertical (y) location of the centre of the streamwise vortices as a function of streamwise distance (x): ●, zero-phase eddy; ○, u-compactness eddy; □, v-compactness eddy. Upper dashed curves are for the wall-to-centreline domain ($y^+ \leqslant 180$), lower solid curves are for the near-wall domain ($y^+ \leqslant 40$).

vortex-centre positions in the wall-to-centreline domain for all three phase determination methods. In the near-wall domain, the compactness conditions result in very similar curves, while the curve for the zero-phase eddy is somewhat lower. In the wall-to-centreline domain, the vortices are seen to be much farther from the wall than in the near-wall domain. At $x = 0$ the vortex centres are at $y^+ = 40$ to 80, depending on the condition used to obtain the phase, while in the near-wall domain, the vortices were at $y^+ = 20$–30. The vortices resulting from the compactness conditions are farther from the wall than for the zero-phase eddy. As in the near-wall domain, the vortices are inclined at about 10° upstream of $x = 0$. Downstream they are inclined as steeply as 60°. In agreement with the near-wall results, the vortices are not discernible far upstream of $x = 0$, and are near the wall for less than 100 wall units. Note that in both domains the vortices are far from the wall for $x^+ > 30$, but in figures 14 (*b*) and 16 (*b*), there is significant ejection near the wall as far downstream as $x^+ = 180$. Thus, the far downstream ejection is below the streamwise vortex pair but is not straddled by them. Also, the inclined vortices observed here are probably related to, and are certainly consistent with, the hairpin eddies investigated by Moin & Kim (1985).

6. Conclusions

The proper orthogonal decomposition technique has been applied to one-, two- and three-dimensional decompositions of turbulent channel flow. Velocity fields generated by direct numerical simulation (Kim *et al.* 1987) were used to compute the full two-point velocity-correlation tensor, $R_{ij}(r_x, y, y', r_z)$, for this purpose. The technique was used to extract energetic organized structures from turbulence.

Turbulent velocity fields were represented as a randomly weighted sum of the eigenfunctions of R_{ij}. The resulting characteristic eddies were found to contribute as much as 76% to the kinetic energy, and even more to turbulence production. Thus the characteristic eddy indeed has special significance.

Several different techniques were used to determine the Fourier phase coefficients of the characteristic eddy, including bispectral analysis and compactness conditions. The results were qualitatively similar for all techniques; however, there were quantitative differences such as the y-locations of the centres of streamwise vortices observed in the characteristic eddies.

In the two-dimensional case (spanwise and normal to the wall), the characteristic eddies consisted of a narrow ejection region accompanied by a region of low streamwise momentum. These were straddled by a pair of weak counter-rotating vortices. It was found that characteristic eddies computed in the near-wall domain were very similar to the near-wall portions of the characteristic eddies computed in the full wall-to-centreline domain.

Three-dimensional eddies were found to be similar to the two-dimensional eddies in that they consisted of an ejection straddled by weak streamwise vortices. The low-speed streak accompanying the ejection is about 400 wall units long and 50 units wide, while the region of strong vertical velocity is less than 200 wall units long. The counter-rotating vortices are inclined at 10° near the wall and as much as 60° away from the wall, and have a streamwise extent in the near-wall region ($y^+ < 40$) of less than 100 wall units. It was noted that while the streamwise vortices occurred in pairs, this did not imply that vortex pairs were in fact dominant in the instantaneous fields since the *pairs* were a result of symmetries in the statistics and the techniques by which the phases were determined. In fact, as noted in §5, solitary inclined vortices rather than pairs are most often observed near the wall in instantaneous velocity fields (Moser & Moin 1984).

The relationship of the characteristic eddies to structures observable in instantaneous flow fields is not clear, though it was demonstrated that the instantaneous structure associated with a large peak in the scattering function did have some qualitative similarity to the characteristic eddy. Presumably, the characteristic eddy represents some average of the most energetic events. It is clear, however, that if the stochastic velocity field is composed of a single structure distributed in the homogeneous directions by a *known* scattering process, then the technique would extract that structure. Also, if the proper orthogonal decomposition eigenfunctions are indeed dominant, and if the scattering process is an impulse process (see the Appendix) with not too densely spaced impulses, then the characteristic eddies would be visible in the flow.

The structures in the instantaneous velocity fields are evolving in time. Unfortunately the three-dimensional characteristic-eddy decomposition performed here does not recover these dynamics. An assessment of the role of the structures in the physics of near-wall turbulence requires some knowledge of their evolution. The treatment of the dynamics of structures obtained by characteristic-eddy decomposition is a topic of continuing research (e.g. Aubry *et al.* 1988).

However, whether the characteristic eddy is actually found in the instantaneous flow field and if so at what frequency may not be the important question. If the main objective of a study of coherent structures is to find a decomposition of turbulence into deterministic and stochastic portions the characteristic-eddy decomposition is certainly the most efficient method in the sense that energy and Reynolds stresses are reproduced with the fewest number of terms ('eddies'). In addition, governing

equations for the coefficients of the characteristic-eddy eigenfunctions can be derived from the Navier–Stokes equations, which is a useful point for theoretical development. Other decompositions are also possible, for example one could easily find the structures that are the most efficient contributors to the magnitude of vorticity fluctuations (Moser 1988).

We are grateful to Drs Robert S. Rogallo and Sanjiva Lele for useful comments on a draft of this manuscript.

Appendix

In §4 it was shown that several quantities had to be specified to fully determine ϕ_i^c in (4.6). In particular, the second-order moments of the stochastic process g were specified (equation (4.8)). To determine the Fourier phases we would have also liked to specify the third-order moments of g by requiring the bispectrum B_g to be a real constant. In this Appendix we examine the physical consequences of these specifications of the statistics of the process g. These statistical properties ((4.8), and B_g a real constant) are shared by many stochastic processes with vastly differing characters. In particular, processes that are *independent* on non-overlapping intervals satisfy these conditions. Two well-studied examples of such processes in one dimension (x) are the Gaussian white-noise process and the Poisson impulse process. Gaussian white-noise is a model for the velocity of a particle undergoing Brownian motion (note that B_g is zero in this case). The Poisson impulse process is the g process used by Rice (1944) in the 'shot-noise' decomposition. The Poisson impulse process can be written

$$g(x) = \sum_j \delta(x - x_j) \tag{A 1}$$

(Papoulis 1965), where x_j are random locations with uniform density along the x-axis. More specifically, the spacings between points are independent and exponentially distributed (this is necessary for the independent-intervals property). The sample functions of these two processes have greatly differing characters. Thus the lower-order statistical properties specified for g do not tell us very much about the sample functions of g.

The Poisson impulse process is particularly interesting in connection with the current problem. If g in (4.8) is indeed an impulse process, then the stochastic process $u_i^{(1)}$ can be interpreted as the sum of characteristic eddies ϕ_i^c occurring at discrete random locations in the homogeneous directions. This is attractive since, if the eddies are not too close together, they would actually be observable in the realizations of $u_i^{(1)}$, and perhaps in u_i. It would thus be appropriate to require that g be an impulse process; that is, a process whose sample functions consist entirely of Dirac delta functions. An impulse process can be considerably more general than the Poisson process; in one dimension, a more general impulse process is

$$g(x) = \sum_j b_j \delta(x - x_j), \tag{A 2}$$

where the b_j are not necessarily independent random variables, and the spacings between neighbouring points x_j are neither independent nor exponentially distributed. If it is arranged so that this process is homogeneous (as we require), its two-point correlation function would be given as

$$\langle g(x)\, g(x + r_x)\rangle = \nu \langle b^2\rangle \delta(r_x) + S(r_x) R_b(r_x), \tag{A 3}$$

where ν is the average density of points, $S(r_x)\,\mathrm{d}r_x$ is the probability that there is a point in the interval $(r_x, r_x+\mathrm{d}r_x)$ given that there is point at 0; and $R_b(r_x)$ is the correlation of the strength b of two impulses separated by a distance r_x. As was discussed in the previous paragraph the statistical conditions ((4.8), and B_g a real constant) are certainly not sufficient to guarantee that g is an impulse process, and (A 3) shows that they are not necessary either. Thus if our goal is to require that g be an impulse process, these specifications are not appropriate.

In general, it is not possible to require that g be an impulse process and satisfy (4.8), except in the limit of impulses that are dense in x. It may however be possible to ask that g be an impulse process in some approximate sense. For example g in one dimension could be further decomposed to $g(x) = g_1(x)+g_2(x)$, where g_1 is an impulse process. This might be accomplished by requiring that

$$\left\langle \left(a_1(x) - \int f(x-\chi)\, g_1(\chi)\, \mathrm{d}\chi \right)^2 \right\rangle \tag{A 4}$$

be a minimum. This was done by Chambers (1987) for a very restricted class of impulse processes g_1. There are difficulties with this minimization problem since it should always be possible to reduce the error (A 4) by increasing the average density of points in g_1. However, allowing an arbitrarily large density of points is undesirable since the structures would then significantly overlap. It is also not clear how such a minimization might be accomplished in practice.

Since we are interested in g being as close as possible to an impulse process, it is interesting to see how well the sample functions of g determined from the conditions in §4 approximate delta functions. To this end, some sample functions of $g(z)$ from the two-dimensional case were computed from sample functions of a_1 using (4.7b). An example is shown in figure 12(a). The sample function is certainly not made up of delta functions. However, it does exhibit regions of intense activity separated by regions of relative calm, and there are occasional very large, short duration excursions. This gives some indication that a decomposition of g into an impulse process and a remainder as discussed above might be a viable approach.

REFERENCES

Adrian, R. J. & Moin, P. 1988 Stochastic estimation of organized turbulent structure: homogeneous shear flow. *J. Fluid Mech.* **190**, 531–559.

Adrian, R. J., Moin, P. & Moser, R. D. 1987 Stochastic estimation of conditional eddies in turbulent channel flow. *Proc. 1987 Summer Program of the Center for Turbulence Research, CTR-S87*, p. 7.

Ahmed, N. & Rao, K. R. 1975 *Orthogonal Transforms for Digital Signal Processing*. Springer.

Aubry, N., Holmes, P., Lumley, J. L. & Stone, E. 1988 The dynamics of coherent structures in the wall region of a turbulent boundary layer. *J. Fluid Mech.* **192**, 115–173.

Aubry, N. & Keefe, L. R. 1987 A low dimensional dynamical system for the wall layer. *Proc. 1987 Summer Program of the Center for Turbulence Research, CTR-S87*, p. 21.

Bakewell, H. P. & Lumley, J. L. 1967 Viscous sublayer and adjacent wall region in turbulent pipe flow. *Phys. Fluids* **10**, 1880–1889.

Bartelt, H., Lohmann, A. W. & Wirnitzer, B. 1984 Phase and amplitude recovery from bispectra. *Appl. Opt.* **23**, 3121–3129.

Blackwelder, R. F. & Eckelmann, H. 1979 Streamwise vortices associated with the bursting phenomenon. *J. Fluid Mech.* **94**, 577–594.

Blackwelder, R. F. & Kaplan, R. E. 1976 On the wall structure of the turbulent boundary layer. *J. Fluid Mech.* **76**, 89–112.

CANTWELL, B. J. 1981 Organized motion in turbulent flow. *Ann. Rev. Fluid Mech.* **13**, 457–515.

CHAMBERS, D. H. 1987 Statistical representation of coherent structures in turbulent flow fields. Thesis, University of Illinois, Champaign-Urbana.

ELGAR, S. & GUZA, R. T. 1985 Shoaling gravity waves: comparisons between field observations, linear theory, and nonlinear model. *J. Fluid Mech.* **158**, 47–70.

FALCO, R. E. 1977 Coherent motions in the outer region of turbulent boundary layers. *Phys. Fluids* **12**, 426.

GLAUSER, M. N., LEIB, S. J. & GEORGE, W. K. 1985 Coherent structures in the axisymmetric turbulent jet mixing layer. *Fifth Symp. on Turbulent Shear Flows, August 7–9, Ithaca NY.*

GRANT, H. L. 1958 The large eddies of turbulent motion. *J. Fluid Mech.* **4**, 149–190.

HERZOG, S. 1986 The large scale structure in the near-wall region of turbulent pipe flow. Thesis, Cornell University.

KIM, J., MOIN, P. & MOSER, R. 1987 Turbulence in fully developed channel flow at low Reynolds number. *J. Fluid Mech.* **177**, 133–166.

KLINE, S. J., REYNOLDS, W. C., SCHRAUB, F. A. & RUNSTADLER, P. W. 1967 The structure of turbulent boundary layers. *J. Fluid Mech.* **30**, 741–773.

LII, K. S., ROSENBLATT, M. & VAN ATTA, C. 1976 Bispectral measurements in turbulence. *J. Fluid Mech.* **77**, 45–62.

LOEVE, M. M. 1955 *Probability Theory*. Van Nostrand.

LUMLEY, J. L. 1967 The structure of inhomogeneous turbulent flows. In *Atmospheric Turbulence and Radio Wave Propagation* (ed. A. M. Yaglom & V. I. Tatarsky), p. 166. Moscow: Nauka.

LUMLEY, J. L. 1970 *Stochastic Tools in Turbulence*. Academic.

LUMLEY, J. L. 1981 Coherent structures in turbulence. In *Transition and Turbulence* (ed. R. E. Meyer), pp. 215–241. Academic.

MATSUOKA, T. & ULRYCH, T. L. 1984 Phase estimation using the bispectrum. *Proc. IEEE.* **72**, 1403–1411.

MOIN, P. 1984 Probing turbulence via large eddy simulation. *AIAA*-84-0174.

MOIN, P. & KIM, J. 1985 The structure of the vorticity field in turbulent channel flow. Part 1. Analysis of instantaneous fields and statistical correlations. *J. Fluid Mech.* **155**, 441–464.

MOSER, R. D. 1988 Statistical analysis of near-wall structures in turbulent channel flow. *Proc. Zaric Memorial Intl Seminar on Wall Turbulence, May 16–20, 1988, Dubrovnik Yogoslavia.*

MOSER, R. D. & MOIN, P. 1984 The effects of curvature in wall-bounded turbulent flows. *NASA TM* 85974.

OBLED, C. & CREUTIN, J. D. 1986 Some developments in the use of empirical orthogonal functions for mapping meteorological fields. *J. Climate Appl. Met.* **25**, 1189.

PAPOULIS, A. 1965 *Probability, Random Variables, and Stochastic Processes*. McGraw-Hill.

PAYNE, F. R. 1966 Large eddy structure of the turbulent wake behind a circular cylinder. Thesis, Pennsylvania State University, University Park.

PERRY, A. E. & CHONG, M. S. 1982 On the mechanism of wall turbulence. *J. Fluid Mech.* **119**, 173.

RICE, S. O. 1944 Mathematical analysis of random noise. *Bell System Tech. J.* **23**, 283.

THEODORSEN, T. 1952 Mechanism of turbulence. In *Proc. 2nd Midwestern Conf. on Fluid Mech.* Ohio State University, Columbus, Ohio.

TOWNSEND, A. A. 1956 *The Structure of Turbulent Shear Flow*. Cambridge University Press.

VAN ATTA, C. W. 1979 Bispectral measurements in turbulence computations. In *Proc. Sixth Intl Conf. on Numerical Methods in Fluid Dynamics* (ed. H. Cabannes, M. Holt & V. Rusanov), Springer.

WALLACE, J. M., ECKELMANN, H. & BRODKEY, R. S. 1972 The wall region in turbulent shear flow. *J. Fluid Mech.* **54**, 39–48.